Urban Climate 55 (2024) 101898

Contents lists available at ScienceDirect

Urban Climate

journal homepage: www.elsevier.com/locate/uclim

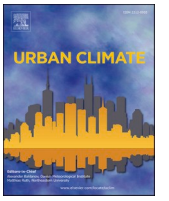

Blue space effects on urban flow and pollution dispersion in a stable atmosphere

Petros Ampatzidis [a,b,*], Carlo Cintolesi [b], Silvana Di Sabatino [b], Tristan Kershaw [a]

[a] Centre for Climate Adaptation & Environment Research, Department of Architecture and Civil Engineering, University of Bath, Claverton Down, BA2 7AY Bath, UK
[b] Department of Physics and Astronomy, University of Bologna, via Irnerio 46, 40126 Bologna, Italy

ARTICLE INFO

Keywords:
Nature-based solutions
Urban blue space
Water evaporation
Pollutant dispersion
OpenFOAM
RANS

ABSTRACT

Investigating solutions capable of mitigating both the Urban Heat and Pollution Islands is key to realising cities that are resilient to climatic change. Stable atmospheric stratification, typical of heatwave events, exacerbates the heat island effect and increases the risk to human health and wellbeing. Here we examine for the first time the mitigation effects induced by waterbodies within an idealised urban neighbourhood under such conditions using RANS simulations. Results show that, in the presence of waterbodies, increased stability enhances the main vortex in the urban canyon, but suppresses the height up to which convective effects are felt. The cooler the waterbody, the greater its cooling effectiveness at street level, whereas the warmer the waterbody, the smaller the area of influence. Under increased stability, the presence of waterbodies leads to the formation of areas with both cooling and warming effects. Warm waterbodies that do not generate a thermal plume strong enough to penetrate the canopy layer can lead up to a 100% increase in pollutant concentrations at street level in some areas, worsening the impact on human health. Urban planners and practitioners should, therefore, consider both the positive effects and unexpected consequences linked to the presence of blue spaces.

1. Introduction

Climate change and increasing urbanisation have and will continue to have severe implications for human health and wellbeing (Watts et al., 2021), exacerbating the effects of the Urban Heat Island (UHI) and Urban Pollution Island (UPI) phenomena. The former refers to the characteristic warmth of cities compared to their rural surroundings and is the single most documented phenomenon of climate change in cities (Santamouris, 2015). The latter is a term that has been gaining traction recently and is introduced in analogy with the UHI, referring to the increased concentration of pollutants in cities (Crutzen, 2004; Li et al., 2018; Di Sabatino et al., 2020). In the UK, it is estimated that heat-related deaths will more than triple by 2050 as a result of climate change, reaching 7000 per year (Environmental Audit, 2018). At the same time, air pollution is the cause of many excess deaths despite efforts to reduce emissions in many urban areas. Particulate matter, for instance, was culpable for more than 200,000 premature deaths in Europe (EU-27) in 2020 (EEA, 2022). It is clear that these risks to human health and wellbeing from the urban anthroposphere need to be addressed along with ongoing efforts to mitigate carbon emissions and promote resource efficiency in urban areas.

* Corresponding author at: Centre for Climate Adaptation & Environment Research, Department of Architecture and Civil Engineering, University of Bath, Claverton Down, BA2 7AY Bath, UK.
E-mail address: p.ampatzidis@bath.ac.uk (P. Ampatzidis).

https://doi.org/10.1016/j.uclim.2024.101898
Received 21 September 2023; Received in revised form 19 December 2023; Accepted 30 March 2024
Available online 8 April 2024

Nature-based solutions (NBS) have emerged as a powerful tool to adapt to and mitigate the effects of climate change, while at the same time enhancing biodiversity and citizens' wellbeing (Frantzeskaki et al., 2019; Girardin et al., 2021; Debele et al., 2023). Our ability to understand and model the thermal and dynamic interaction of various green (e.g. parks, trees and green roofs) or blue (e.g. ponds, lakes and rivers) NBS with their urban surroundings is integral for the formation of comprehensive solutions to the challenges of the UHI and UPI. The incorporation of blue spaces for the amelioration of the urban climate is a new emerging field as the focus of recent advances on NBS has been almost exclusively directed towards green NBS. However, our understanding of and ability to accurately model the processes and phenomena that dictate the thermal behaviour of blue spaces within an urban context remains limited (Gunawardena et al., 2017; Ampatzidis and Kershaw, 2020).

One aspect of urban flow that is related to the magnitude of the UHI (Schrijvers et al., 2015) and has serious implications for the dispersion of pollutants in cities is thermal stratification (Kanda and Yamao, 2016; Marucci and Carpentieri, 2020a; Zhao et al., 2020). A distinction should be made between the local and background thermal stratification of the atmospheric boundary layer (ABL). The former refers to thermal effects induced by differential heating of urban surfaces such as the ground, buildings and roofs (Allegrini et al., 2013; Barbano et al., 2021; Cintolesi et al., 2021a); the latter refers to variations in atmospheric temperature with height. Although most of the existing urban studies—that is, studies of the urban climate that do not consider the presence of water-bodies—focus on local buoyancy effects (Zhao et al., 2020), recent field and experimental studies (Marucci et al., 2018; Marucci and Carpentieri, 2019) and advances in numerical modelling (Grylls et al., 2020; Zhou et al., 2021) have highlighted the crucial role of atmospheric stability on the urban climate. The depth of the urban boundary layer, the velocity and temperature fields, as well as the turbulence properties in an urban area, are all factors dependent upon the thermal stratification of the atmosphere: if the ABL is thermally neutral, stably, or unstably stratified. For instance, a weak UHI is usually related to convectively unstable daytime conditions, i.e. when the air temperature decreases with altitude at a higher rate than normal, whereas a strong UHI is mostly found during calm nights with increased stability and lower mixing depths (Oke et al., 2017), i.e. when a warm layer of air is sitting on top of a cooler one inhibiting vertical mixing and dispersion of pollutants. The importance of evaluating blue space performance within a stable background atmosphere is further highlighted by the fact that night-time heatwaves exhibit greater increases in frequency than daytime heatwaves (Wu et al., 2023). Nonetheless, the vast majority of the existing literature that concerns the impact of waterbodies on the urban climate ignores atmospheric stratification effects, typically assuming neutral conditions.

Green spaces such as parks, trees, or green roofs have been shown to promote mixing or absorb gaseous pollutants through leaf stomata and thus reduce pollutant concentration levels locally (Selmi et al., 2016; Abhijith et al., 2017; Buccolieri et al., 2011; Abhijith and Kumar, 2020). However, research on the potential to mitigate air pollution with blue spaces is scarce (Kadaverugu et al., 2022). Studies have looked at how urban waterbodies can abate air pollution through wet deposition, the process by which gaseous pollutants mix with suspended water in the atmosphere and are then deposited on the water surface (Zhao et al., 2021; Fan et al., 2022), but there is currently a lack of knowledge on how urban blue space can enhance pollutant dispersion. Past studies have looked at the influence of the breeze system induced by large bodies of water (e.g. the Great Lakes) on the concentration of pollutants in neighbouring urban areas, indicating a worsening of pollution levels (Lyons and Olsson, 1973; Indumati et al., 2009). Nonetheless, these studies have only considered large waterbodies that are known to create large recirculation regions and exhibit small temperature variations of the year. Recent evidence suggests that under calm weather and during late summer nights—when small urban waterbodies can become warmer than the surrounding air—blue space can promote vertical mixing and enhance the dispersion of pollutants (Ampatzidis et al., 2023). However, this is inconclusive as, to the best of the authors' knowledge, the assessment of pollutant dispersion by waterbodies in a stable atmosphere has not been considered in similar works.

From an experimental point of view, it has been shown that under stable stratification, pollutants tend to accumulate in the wake of buildings, as increased stability tends to hamper turbulent mixing with the atmosphere above (Yassin, 2013), leading to elevated concentration levels compared to cases under neutral conditions (Marucci and Carpentieri, 2020b,a). On the contrary, unstable stratification enhances the production of turbulent kinetic energy (TKE or k) and turbulent kinetic fluxes of pollutants around buildings, thus decreasing the concentration of pollutants within urban canyons (Li et al., 2010; Marucci and Carpentieri, 2020a). Numerical studies, particularly computational fluid dynamics (CFD) simulations that have become widespread when a careful analysis of physical processes is required (Di Sabatino et al., 2007), also highlight the effects of a thermally stratified atmosphere on pollutant dispersion in urban environments (Xie et al., 2013; Zhao et al., 2020). For instance, it is shown that greater concentrations were observed with increasing strength of stable stratification due to the suppression of turbulence and decrease of vertical pollutant fluxes above the urban canopy (Sessa et al., 2020). Despite recent advances in computational resources, Reynolds-Averaged Navier-Stokes (RANS) simulations are still preferred by many researchers over the more accurate, but much more computationally expensive, Large-Eddy Simulations (LES). RANS simulations are known for their ability to reproduce complex geometries and realistic flows at high Reynolds numbers, with sufficient accuracy, especially for what concerns the mean flow and the overall flow features. It has also been shown that both approaches can accurately reproduce the fluid dynamics of problems concerning dispersion, with LES being more accurate in simulating dispersion mechanisms that depend on intermittent, non-stationary fluctuations (Salim et al., 2011).

This paper addresses the existing research gaps by investigating for the first time blue space effects under stable thermal stratification—typical of heatwaves events—and by accounting for pollutant dispersion within an urban context. This is achieved by extending our previous work presented in Ampatzidis et al. (2022, 2023) where novel RANS simulations, accounting for evaporation and heat transfer from water, were employed to evaluate changes in the flow structure and temperature field under neutral conditions. In this paper, we further develop the model via the incorporation of the Monin-Obukhov Similarity Theory (MOST) and the consideration of pollutant dispersion. Three different strengths of stability, including neutral conditions for comparison, are considered and simulated against scenarios where the water is cooler and warmer than its surroundings. The geometry of the case study is similar to Ampatzidis et al. (2022, 2023), i.e. a uniform 7×3 building array, where the central building is removed and replaced by a square

evaporating waterbody, resembling an open square configuration (Fig. 1a).

2. Simulation approach

2.1. Governing equations

The ambient air is modelled as a mixture of ideal gases composed of dry air and water vapour. The onset of buoyancy is taken into account via the Boussinesq approximation, which depends on gradients of temperature, T [K], and vapour concentration, q [−]. In this framework, the governing equations read:

$$\frac{\partial u_j}{\partial x_j} = 0, \tag{1}$$

$$\frac{\partial u_i}{\partial t} + \frac{\partial u_j u_i}{\partial x_j} = -\frac{1}{\rho_0}\frac{\partial p}{\partial x_i} + \nu \frac{\partial^2 u_i}{\partial x_j \partial x_j} + b_i, \tag{2}$$

$$b_i = g_i\left(1 - \beta_T \Delta T - \beta_q \Delta q\right), \tag{3}$$

where u_i are the velocity components [m s^{-1}], p is the pressure [Pa], ρ_0 is the reference fluid density [kg m^{-3}], ν is the molecular kinematic viscosity [m^2 s^{-1}], b_i is the buoyancy force [m s^{-2}], and g_i is the gravitational acceleration vector [m s^{-2}]. Buoyancy is expressed in terms of the variation of temperature $\Delta T = T - T_0$ and vapour concentration $\Delta q = q - q_0$ with respect to the reference values (T_0 and q_0, respectively) and their volume expansion coefficients β_T [K^{-1}] and β_q [−]. The equations for temperature and water vapour concentration read:

$$\frac{\partial T}{\partial t} + \frac{\partial}{\partial x_i}(T u_i) - \alpha_T \frac{\partial^2 T}{\partial x_j \partial x_j} = S_e, \tag{4}$$

$$\frac{\partial q}{\partial t} + \frac{\partial}{\partial x_i}(q u_i) - \alpha_q \frac{\partial^2 q}{\partial x_j \partial x_j} = 0, \tag{5}$$

where α_T and α_q are the molecular diffusivities of air and water vapour, respectively, and S_e is the evaporation heat sink term which is given by the water change of phase. The pollutant concentration C is modelled as a passive scalar and is governed by:

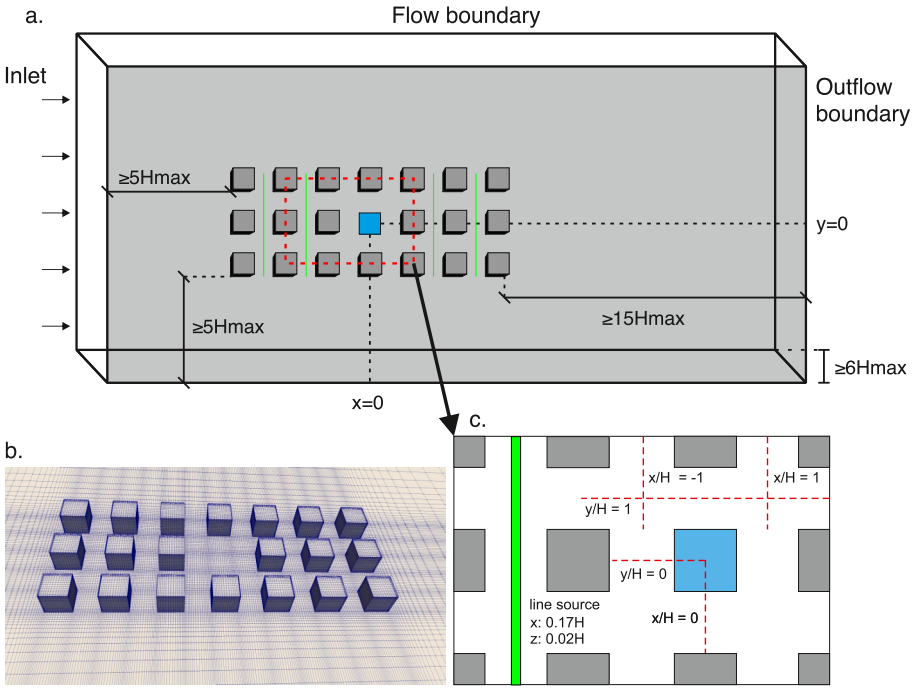

Fig. 1. (a) Schematic representation of the case geometry. Green lines indicate the location of ground–level pollutant line sources. (b) Sketch of the computational grid. (c) Ground–level pollutant line sources and sampling lines used for the analysis of the results. (For interpretation of the references to colour in this figure legend, the reader is referred to the web version of this article.)

$$\frac{\partial C}{\partial t}+\frac{\partial}{\partial x_j}(Cu_i)-D\frac{\partial^2 C}{\partial x_k \partial x_k}=0, \tag{6}$$

where D is the diffusion coefficient [$m^2\ s^{-1}$] and g the gravity acceleration.

2.2. Evaporation model

This paper adopts the evaporation model proposed in Cintolesi et al. (2016, 2017) and adapted for RANS simulations by Ampatzidis et al. (2022). The blue space is considered to be at rest with a uniform and constant surface temperature, representing a well-mixed and shallow urban waterbody. Thus, the reproduction of the internal motions of water is beyond the scope of this study. Rather, the thin-film assumption is used to model water surface evaporation: the free surface of the water body is modelled as a wet surface that can evaporate infinitely, acting as a source of water vapour (Petronio, 2010).

The evaporation velocity, u_q [ms^{-1}], is modelled by adopting a semi-impermeable model that is dependent on the water vapour gradient in the direction normal to the water surface (Welty et al., 2007):

$$u_{q,i}=-\frac{\alpha_q}{1-q_\Gamma}\left(\frac{dq}{dn_i}\bigg|_\Gamma\right)n_i, \tag{7}$$

where the subscript Γ indicates that the quantities are evaluated at the air-water interface, and n_i is the vector normal to the interface pointing into the air domain. The vapour concentration at the interface is computed by an empirical formula:

$$q_\Gamma=\frac{M_v}{M_a}\ \frac{\phi_\Gamma\ p_{sat}(T_\Gamma)}{p-\left(1-\frac{M_v}{M_a}\right)\phi_\Gamma\ p_{sat}(T_\Gamma)}, \tag{8}$$

where $M_a=28.97\ \ g\ mol^{-1}$ and $M_v=18.02\ \ g\ mol^{-1}$ are the molar masses of air and water vapour, ϕ_Γ is the relative humidity at the air-water interface, and p_{sat} is the saturated vapour pressure at the interface. The air-water interface is assumed to be under saturation conditions; thus, the relative humidity at the interface is $\phi_\Gamma=1$. The saturation pressure p_{sat} at the interface is evaluated based on the interface temperature using Buck's formula:

$$p_{sat}(T)=611.85exp\left[\frac{17.502(T-273.15)}{240.9+(T+273.15)}\right]. \tag{9}$$

The heat sink term due to the phase change of water at the air-water interface, S_e, is introduced to account for the energy subtracted from the system due to evaporation in Eq. (4). It is applied numerically to the first cells adjacent to the water surface, whilst it is zero everywhere else; it is computed as follows:

$$S_e=-\frac{\rho^* L_h}{\rho C_p}\frac{\partial u_{q_i}}{\partial x_i}, \tag{10}$$

where ρ^* [$kg\ m^{-3}$] is the density of the mixture of air and water vapour, which is taken equal to the density of air with reasonable accuracy (Çengel and Ghajar, 2015), L_h [$J\ kg^{-1}$] is the latent heat of vaporisation, and ρC_p [$J\ m^{-3}\ K$] is the volumetric heat capacity.

A more detailed description of the evaporation model can be found in Petronio (2010), Sosnowski et al. (2013) and Cintolesi et al. (2016, 2017).

2.3. Inlet thermal stratification

The reproduction of thermally stratified inlet profiles for velocity and temperature is achieved through the MOST. One of the breakthroughs in urban climate research was the observation that MOST is applicable in the inertial sublayer above cities (Roth, 2000). MOST can be utilised to extend the logarithmic profiles proposed by Richards and Hoxey (1993)—and later revisited by Richards and Norris (2011)—for a neutral atmospheric boundary layer to a generalised form accounting for non-isothermal conditions. However, these equations contain dimensionless stability functions that are usually determined by fitting with observations. As this study concerns a scale model and an idealised geometry we are not interested in reproducing real heatwave events; rather, our aim is to investigate the behaviour of waterbodies under conditions representative of typical conditions in an urban context. Therefore, in this study, we adopt the parametrisation presented in Marucci et al. (2018), where the authors fitted the stability functions with the experimental profiles of their wind tunnel study. For a stable stratification, the MOST equations read:

$$U(z)=\frac{u_*}{\kappa}\left[ln\left(\frac{z'}{z_0}\right)+8\frac{z'-z_0}{L}\right], \tag{11}$$

$$T(z)=T_G+\frac{\theta_*}{\kappa}\left[ln\left(\frac{z'}{z_{0h}}\right)+16\frac{z'-z_{0h}}{L}\right], \tag{12}$$

where u_* [m s^{-1}] is the friction velocity, $z^{'} = z - d$ where z [m] is the vertical coordinate component and d is the displacement height (here taken as $d = 0$), z_0 [m] is the aerodynamic roughness length, z_{0h} [m] is the thermal roughness length, $\kappa = 0.4$ [−] is the von Karman constant, T_G [K] is the temperature of the ground, and L [m] is the Monin-Obukhov length, a length scale analogous to the ratio of mechanical and thermal forces:

$$L = \frac{\overline{\theta} u_*^2}{\kappa g \theta_*}, \tag{13}$$

where θ_* [K] is the friction temperature.

2.4. Dimensionless parameters for non-isothermal conditions

This study refers to the strength of the stable background thermal stratification using the stability parameter (Oke et al., 2017), $\zeta = z^{'}/L$. The shift between a stable and a very stable boundary layer occurs at $\zeta = 1$. Values ranging $0 < \zeta < 1$ are considered stable while for $\zeta > 1$ a very stable stratification is formed Oke et al. (2017). A local Richardson number is introduced to describe the dynamic stability and the convection regimes within the street canyon under consideration by taking into account the thermal contributions due to natural convection and the buoyancy effects of an evaporating waterbody.

$$Ri = \frac{Gr}{Re_H^2}, \tag{14}$$

where $Re_H = U_H H/\nu$ is the Reynolds number at building height H, U_H is the inlet velocity at the building's height, and Gr is the Grashof number. When $Ri \gg 1$, natural convection dominates the overall flow, while when $Ri \ll 1$, forced convection drives the flow. Values between $0.1 < Ri < 5$ can be considered a mixed-convection flow regime for cases concerning evaporation phenomena (Pauken, 1998), i.e. where buoyancy forces have a considerable contribution to the overall flow dynamics.

2.5. Numerical approach and turbulence modelling

The simulations adopt the RANS approach for reproducing turbulent flows. The averaging in time of Eq. (2) introduces the Reynolds stress, whose anisotropic part is modelled using the eddy viscosity hypothesis (Pope, 2013). The $k - \omega$ Shear Stress Transport (SST) turbulence model is employed to close the system (Menter et al., 2003), where ω is the specific dissipation rate. By analogy with the momentum equation, the averaging in time for Eq. (4) and Eq. (5) for temperature and vapour concentration, respectively, leads to the appearance of turbulent flux terms, i.e. $h_i = \langle u_i^{'} T^{'} \rangle$ and $\ell_i = \langle u_i^{'} \omega^{'} \rangle$, respectively. These are modelled using the gradient hypothesis: $h_i = -\alpha_{T,t} \ \partial T/\partial x_i$ and $\ell_i = -\alpha_{\omega,t} \ \partial \omega/\partial x_i$, where the turbulent diffusivity of temperature and water vapour are evaluated through the turbulent Prandtl (Pr_t) and Schmidt (Sc_t) numbers, i.e. $\alpha_{T,t} = \nu_t/Pr_t$ and $\alpha_{\omega,t} = \nu_t/Sc_t$. The wall functions used for the turbulent viscosity, kinematic turbulent thermal conductivity, TKE and specific dissipation rate are *atmNutkWallFunction*, *atmAlphatWallFunction*, *kqRWallFunction* and *atmOmegaWallFunction*. For the turbulent diffusivity of water vapour, a wall function is adopted following Ampatzidis et al. (2022).

The numerical simulations are performed using the open-source CFD software OpenFOAM (ESI-OpenCFD, 2006). The authors have developed an in-house solver to implement the evaporation model presented in Section 2.2. The new solver is based on the steady-state solver *buoyantBoussinesqSimpleFoam* for buoyant, turbulent flow of incompressible fluids provided in OpenFOAM. More details on the implementation of the evaporation model in the solver can be found in Ampatzidis et al. (2022).

3. Validation

The validation of the 3D dynamics of the simulation approach was conducted and presented in Ampatzidis et al. (2022), which considered two cases: flow past a single building and a 3×3 building array. Here, we present the validation of the extended numerical model, which includes atmospheric thermal stratification, against the wind tunnel measurements of Marucci and Carpentieri (2019) (hereafter *MC19*). These experiments aimed to assess the effects of a stable background thermal stratification on flow circulation and pollutant dispersion inside and above a bi-dimensional street canyon. The wind tunnel comprises a 20 m long, 3.5 m wide and 1.5 m high working section. For the reproduction of a stable boundary layer, the floor was cooled using recirculating water while a vertical temperature profile was imposed at the inlet using a series of horizontal heaters placed at different heights. The street canyon has a square section, with height $H = 0.166$ m and width $L = H$, while it extends $L = 15H$ in the spanwise direction. Ground surfaces are heated or cooled through electrical heater mats or circulating water. The case of stable thermal stratification with and without local thermal effects is considered for the validation purposes of the present study. All three cases, i.e. no heating (*NH*), leeward heating (*LH*) and windward heating (*WH*), are reproduced numerically, but only the first two are shown here for brevity.

3.1. Validation case description

The wind tunnel ground temperature is kept constant at $T_G = 19$°C and the temperature difference between the ground and the top of the boundary layer, defined as $5 \times H$, is $\Delta T = 7$°C. The reference velocity is $U_{REF} = 0.65$, while the friction velocity and friction

temperature are given as $u_* = 0.023$ and $\theta_* = 0.12$, respectively. The Reynolds number at building height is $Re_H = 5300$, while the Richardson number is $Ri_H = 0.13$. The temperature at twice the building height is $T_{2H} = 25.1$°C. For cases with a heated wall, a constant temperature of $T_{Hot} = 118$°C is applied at the leeward or windward wall within the canyon.

The computational domain is two-dimensional with a size of $24H \times 9H$ and it is discretised with 272×87 cells in the streamwise (x) and vertical (z) dimensions, respectively. All surfaces of the wind tunnel are simulated as smooth and flat. The flow is driven by interpolated inlet conditions for streamwise velocity and temperature according to the approaching profiles provided in the experiments. For TKE, the inlet profile is evaluated as $0.75\left(\overline{u'^2} + \overline{w'^2}\right)$, as proposed in *MC19*, where u' and w' are the streamwise and vertical velocity fluctuations. The ω profile is estimated as:

$$\omega(z) = \frac{C_\mu^{3/4} k^{1/2}}{l}, \tag{15}$$

where $C_\mu = 0.09$ is a model constant and l is the turbulent length scale estimated as 5% of the inlet boundary layer height for wall-bounded flows. Fig. 2 shows the profiles of the approaching flow.

3.2. First- and second-order statistics

Fig. 3 presents the comparison of the first- and second-order statistics for the *NH*, *LH* and *WH* at the centreline along the streamwise direction, above the buildings, and within the canyon. The quantities are normalised with the velocity and temperature at twice the height of the building, U_{2H} and T_{2H} respectively, and the characteristic difference of temperature which is $\Delta T = T_{2H} - T_G$ for the *NH* case and $\Delta T = T_{Hot} - T_{2H}$ for the *LH* and *WH* cases (T_G is the ground temperature and T_{Hot} is the temperature of the hot building facade). The velocity profiles are accurately reproduced in all cases, whereas the reproduction of TKE shows some underestimation near and above the roof level. For temperature, the profiles almost collapse on the experimental ones, albeit slight discrepancies at the roof level for the *LH* case.

To grasp the overall accuracy of the model, Fig. 4 shows the comparison on 13 selected lines along the streamwise direction. Here, the *WH* case is not shown for simplicity. The range of the normalised quantities is also given for scale. The velocity profiles reproduce with good accuracy the circulation inside and above the canyon in all cases. The profiles of averaged TKE reproduce correctly the experimental data, albeit with a slight underestimation of the peak value in the areas above the building roof $(1 < z/H < 1.5)$ in both cases. Particularly, in the *NH* case, TKE is underestimated at $z/H = 1.1$ above the windward building $(x/H < 0)$, while the agreement improves above the downwind one $(x/H > 0)$. In the *LH* case, the reproduction of TKE is satisfactory, albeit with some discrepancies at the air–canyon interface. For temperature, simulations reproduce accurately the stably stratified temperature field both above and within the street canyon. The *NH* results practically collapse to the experimental ones, whilst the *LH* case exhibits slight inaccuracies at the roof level $(z/H = 1.1)$ and close to the windward facade.

3.3. Statistical metrics

Statistical metrics proposed by the European COST Action 732 (Schatzmann et al., 2010) are used to evaluate the accuracy of the simulations, namely the hit rate, *HR*, the fraction of the prediction within a factor of two observations, *FAC*2, the normalised mean square error, *NMSE*, and the fractional bias, *FB*. The *HR* and *FAC*2 take values in $[0, 1]$, with a value of 1 indicating a perfect match. The threshold values of $HR \geq 0.66$ and $FAC2 \geq 0.5$ are taken as indicators of satisfactory validation. The ideal value for *FB* and *NMSE* is zero, while $|FB| < 0.3$ and $NMSE < 4$ indicate a successful validation. A complete description of the metrics can be found in Schatzmann et al. (2010), while for the adopted threshold parameters the reader is referred to Ampatzidis et al. (2022).

Table 1 presents the calculated metrics for the three simulated cases. Note that the measurement errors reported in the wind tunnel

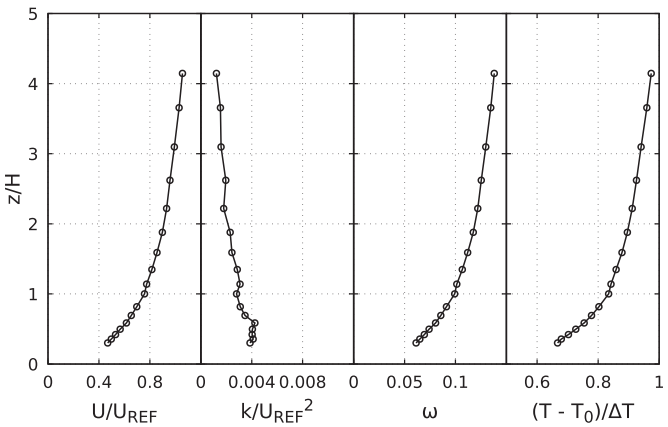

Fig. 2. Vertical profiles of U, k, ω and T of the approaching stable boundary layer.

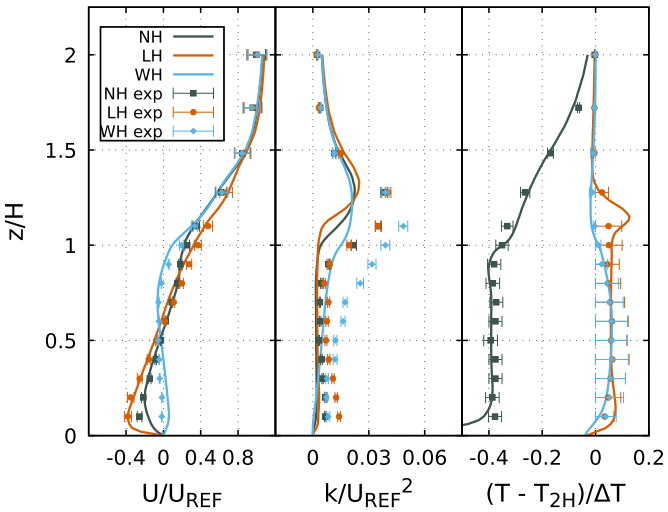

Fig. 3. Vertical profiles of averaged streamwise velocity U, TKE and temperature, T, along the centreline $(x/H = 0)$. Comparison between experimental data with standard error (dots and error bars) from *MC19* and present simulations (lines).

datasets were taken into account in the calculation. Based on the given thresholds of acceptance, the model presents a satisfactory agreement with the wind tunnel experiments given the acknowledged limitations of the RANS approach. Velocity and temperature metrics are all within their respective thresholds, whilst TKE observed less agreement. This is consistent with the results for neutral stratification presented in Ampatzidis et al. (2022), where it was shown that the reproduction of TKE is a shortcoming in the $k-\varepsilon$ (models)

It should be noted that the two cases where local thermal forces are introduced via wall heating are very sensitive to the selection of under-relaxation factors. These are factors introduced to stabilise the simulation by limiting the amount by which a variable changes from the previous iteration to the next one. Careful calibration of the under-relaxation factors for pressure and velocity is needed; otherwise, the simulations might converge to a nonphysical solution. In this study, the selected under-relaxation factors range between 0.05 and 0.15 for pressure, 0.85–0.9 for velocity, 0.15–0.25 for temperature and 0.15–0.2 for the turbulent quantities.

4. Case study description

4.1. Case geometry and computational domain

In this study, the effects of waterbodies, which are either cooler or warmer than their urban surroundings, on airflow and pollutant dispersion are examined by taking into account the influence of neutral and stable ambient thermal stratification. The urban fabric consists of the idealised urban neighbourhood described in Section 1 and shown in Fig. 1. The buildings are cubes, with an edge of $H = 1.5\ m$, located at a distance H from each other. The replacement of the central building with a square waterbody of similar surface area creates an open-square configuration, which resembles open spaces, such as parks, where blue spaces are often encountered in cities. Following the classification by Oke et al. (2017), an isolated roughness flow regime is developed in the open square, while between the buildings, a skimming flow regime is established. This configuration had initially been selected to study the impact of the size and shape of the waterbody, as presented in Ampatzidis et al. (2023). To isolate the influence of the prevailing wind we had to decrease the size and elongate the shape of waterbodies (keeping a constant area). Therefore, a more compact configuration would not allow for this. As a result and for the sake of consistency, we have maintained the same configuration for this study.

The size of the computational domain is decided based on best practise guidelines for flows in the urban environment (Franke et al., 2007; Tominaga et al., 2008), that is, the inlet is located at a distance $5H$ from the building array, the lateral boundaries are located at $7.5H$, the top boundary at $5H$, and the outlet at $15H$ away from the buildings. The final dimensions of the computational domain are $33H \times 35H \times 6H$ in the streamwise, spanwise and vertical directions. The computational grid consists of a structured, orthogonal, and Cartesian mesh consisting of $263 \times 160 \times 51$ cells for a total of 2,033,440 cells. The centre of the first cell in the vertical direction is located closer to the wall at $z = 0.03$ m to ensure $30 \leq y^{+} \leq 300$ for all cases. A grid independence study is carried out on three meshes (Appendix A). The error estimate between the values of the medium and fine mesh is computed using the Grid Convergence Index (Roache, 1994, 1997), which for U and TKE is 0.03% and 0.01%, respectively, indicating that the medium mesh provides nearly grid-independent results.

4.2. Thermal stratification and waterbody temperature

Four simulations without the waterbody have been considered baseline cases. These include a neutral case and three simulations that reproduce different levels of stable thermal stratification of the atmosphere (see Eqs. (11), (12)): *NB*: Neutral baseline (constant air

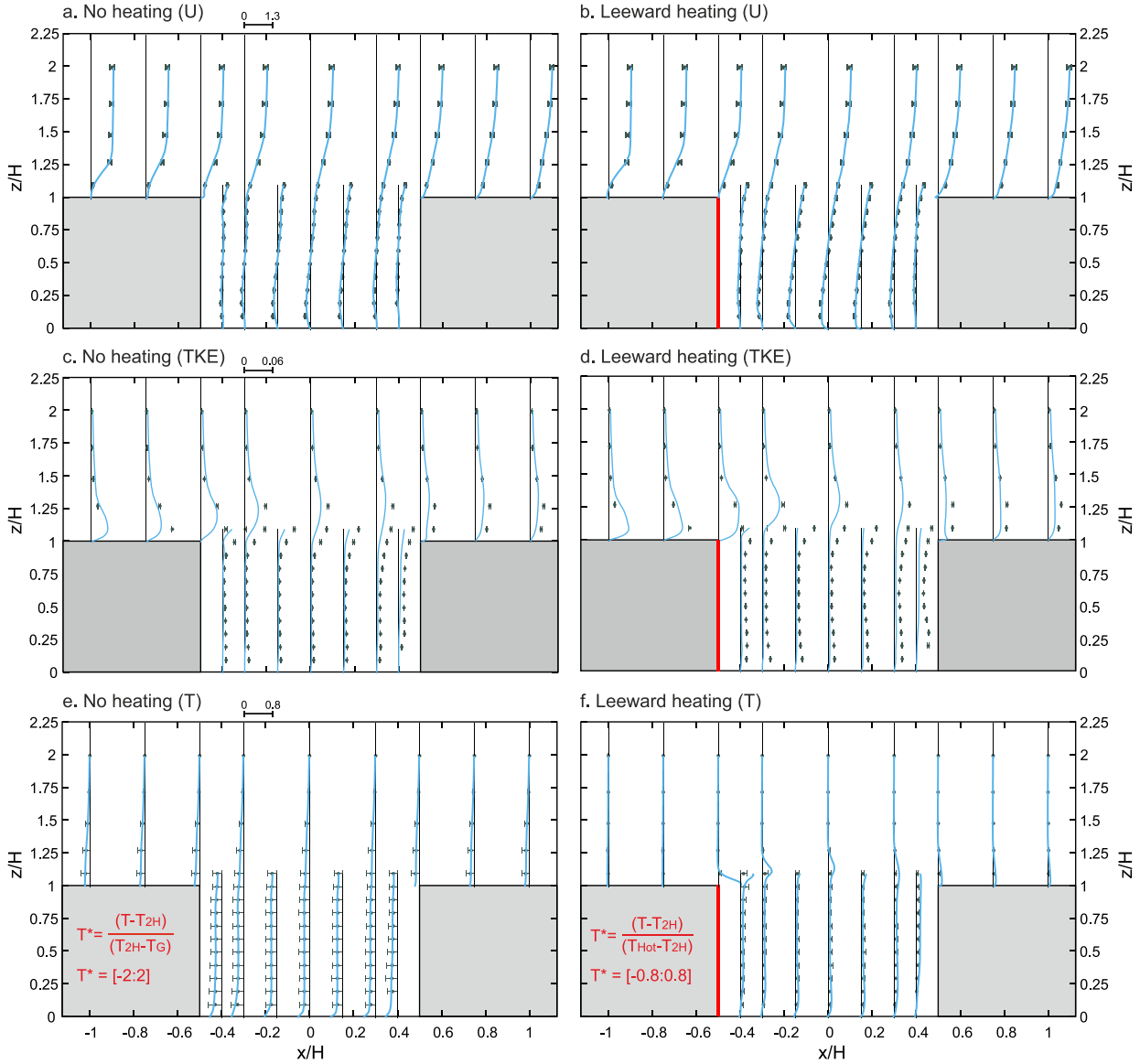

Fig. 4. Vertical profiles of averaged streamwise velocity U, TKE and temperature, T, at 13 locations within and above the street canyon: $x/H = \pm 1$, ± 0.7, ± 0.5, ± 0.4, ± 0.3, ± 0.15, 0. Comparison between experimental data with standard error (dots and error bars) from *MC19* and present simulations (lines). Panel (a, c, e) *NH*: No Heating; (b, d, f) *LH*: Leeward Heating.

Table 1
Validation metrics calculated for the streamwise velocity (U), turbulent kinetic energy (TKE) and temperature (T), along with the relative thresholds. NH: No heating; LH: Leeward wall heated; WH: Windward wall heated.

	U		TKE				T			
	HR	*FAC2*	*HR*	*FAC2*	*NMSE*	*FB*	*HR*	*FAC2*	*NMSE*	*FB*
	≥ 0.66	≥ 0.5	≥ 0.66	≥ 0.5	≤ 4	≤ 0.3	≥ 0.66	≥ 0.5	≤ 4	≤ 0.3
NH	0.70	0.86	0.59	0.40	0.99	−0.59	1	1	0.0001	−0.005
LH	0.68	0.92	0.34	0.22	1.34	−0.63	0.98	1	0.01	0.04
WH	0.65	0.73	0.47	0.47	1.68	−0.73	0.97	0.99	0.02	−0.01

temperature $T_a = 20°C$); *WB*: Weak stability baseline with $\zeta = 0.3$; *MB*: Medium stability baseline with $\zeta = 0.9$; *SB*: Strong stability baseline with $\zeta = 2$;

The *MB* case has been set up using the u_* and θ_* reported in *MC19*; while the weak and strong stratification cases have been imposed by modifying the value of the gravitational acceleration and keeping the other boundary conditions fixed, as suggested in Boppana et al. (2013) and Sessa et al. (2020). The temperature difference between the building height and the ground is $\Delta T = 4.4$ °C, 5 °C and 6 °C, from the weakest to the strongest stabilities, respectively. The scaling parameters of the four baseline boundary layers are reported in Table 2.

A single square waterbody is introduced in the middle of the open square (Fig. 1a) and its thermal interaction with the urban surroundings is examined with respect to the atmosphere's stratification level. For the neutral case, the waterbody is selected to be 4°C and 8°C cooler and warmer than the air temperature. For the cases under increased stability, as the background atmosphere is stably stratified—with in-canyon temperature differences ranging from 4.4 °C to 6 °C—the selection of the water temperature is not as straightforward as it is for the neutral conditions. One would expect different results if the water is cooler or warmer with respect to the ground, the buildings, the air just above the water surface or the air at building height and the free stream. Here, for the cooler-waterbody cases, the water temperatures are set with respect to the ground temperature, which is constant at $T_G = 20^{\circ}$C in all cases. Similarly to the neutral cases, two cool water temperatures are considered, namely $\Delta T_{G-w} = -4^{\circ}$C and $\Delta T_{G-w} = -8^{\circ}$C. For the warmer-waterbody cases though, the water temperature is set to be warmer than the temperature at building height. This can be justified by the fact that we are particularly interested in investigating the potential of warmer waterbodies for breaking up the interface at roof level and promoting vertical transport of air and pollutants (Ampatzidis et al., 2022, 2023). However, since the stable boundary layers under consideration lead to different temperatures at building height, the water temperature varies accordingly to maintain a similar temperature difference, ΔT_{H-w}, in all cases. Two warm water temperatures are considered, namely $\Delta T_{H-w} = +4^{\circ}$C and $\Delta T_{H-w} = +8^{\circ}$C. A summary of the local scaling quantities of each case can be found in Table 3.

It is worth noting here that the main focus of this study is to assess the interaction of waterbodies with the urban surroundings under stable stratification at a snapshot in time, indicative of nocturnal conditions in a heatwave. In the UK, the Health Security Agency provides key trigger temperatures for different regions across the country, with the threshold for night-time temperatures varying between 15 °C and 18 °C—the latter set for London (UKHSA, 2022). Therefore, the selected temperatures—minimum of 20 °C at the ground (Table 3)—can be considered typical of heatwave events. The scaling-up exercise of selected cases presented in Table 4 shows that temperatures above the heatwave thresholds would be maintained for a full-scale model and that the imposed air-water temperature differences are similar to the ones observed in the urban environment (Yao et al., 2023).

4.3. Kinematic and thermal boundary conditions

The idealised neighbourhood is exposed to a constant turbulent and thermally stratified flow. The boundary conditions for the neutral case are set similarly to Ampatzidis et al. (2022). At the inlet, the profiles of U, k and ω are set based on the equations for a neutrally stratified flow proposed by Richards and Hoxey (1993); Richards and Norris (2011). For the cases under stable thermal stratification, the profiles of U and T, as described in Eq. (11) and Eq. (12), are imposed at the inlet respectively. The inlet profile of k is estimated based on the proposed equation by Guo et al. (2021):

$$k(z) = \frac{u_*^2}{\sqrt{C_\mu}}\left(\frac{1+4z}{1+5z}\right), \tag{16}$$

where u_* $\left[\mathrm{m\,s^{-1}}\right]$ is the friction velocity, C_μ is a model constant taken equal to $C_\mu = 0.09$ and z [m] is the vertical height. The inlet profile for the specific turbulent dissipation rate, ω, follows Eq. (15). For vapour concentration, a constant value is set at the inlet based

Table 2
Nominal scaling parameters for the three approaching stable boundary layers under consideration. *WB*: weak stability baseline ($\zeta = 0.3$); *MB*: medium stability baseline ($\zeta = 0.9$); *SB*: strong stability baseline ($\zeta = 2.0$).

	NB	*WB*	*MB*	*SB*
U_{ref} $\left[\mathrm{m\,s^{-1}}\right]$	0.8	0.8	1	1.5
u_* $\left[\mathrm{m\,s^{-1}}\right]$	0.128	0.112	0.112	0.112
g $\left[\mathrm{m\,s^{-2}}\right]$	9.81	3.5	9.81	21
z_0 [m]	0.135	0.135	0.135	0.135
θ_* [°C]	–	0.12	0.12	0.12
z_h [m]	–	1.2×10^{-6}	1.2×10^{-6}	1.2×10^{-6}
L [m]	∞	22.5	8	3.7
T_a [°C]	20	Eq. (12)	Eq. (12)	Eq. (12)
T_G [°C]	20	20	20	20
ΔT_{H-G} [°C]	–	4.4	5	6
ΔT_{max} [°C]	–	6.2	9	14
ζ	–	0.3	0.9	2.0
Re_H	7.9×10^4	7.9×10^4	9.9×10^4	1.5×10^5
Re^*	1143	1000	1000	1000

Table 3
Local scaling quantities at the street canyon level for all the simulated cases.

	ζ [−]	U_H [m s^{-1}]	T_H [°C]	T_G [°C]	T_w [°C]	Ri [−]
NB	–	0.8	20	20	–	–
*NC*4	–	0.8	20	20	16	0.31
*NC*8	–	0.8	20	20	12	0.63
*NW*4	–	0.8	20	20	24	0.43
*NW*8	–	0.8	20	20	28	0.80
WB	0.3	0.8	23.6	20	–	–
*WC*4	0.3	0.8	23.6	20	16	0.21
*WC*8	0.3	0.8	23.6	20	12	0.33
*WW*4	0.3	0.8	23.6	20	27.6	0.16
*WW*8	0.3	0.8	23.6	20	31.6	0.30
SB	2	1.5	25.2	20	–	–
*SC*4	2	1.5	25.2	20	16	0.51
*SC*8	2	1.5	25.2	20	12	0.72
*SW*4	2	1.5	25.2	20	29.2	0.24
*SW*8	2	1.5	25.2	20	33.2	0.48

Table 4
Example of the implementation of a *Ri* number scaling following Tsalicoglou et al. (2020), and assuming wind speeds between 3 ms^{-1} and 4 ms^{-1} as typical values for urban areas.

		H [m]	U_H [m s^{-1}]	g [m s^{-2}]	T_H [°C]	T_G [°C]	T_w [°C]	Ri_L
WW4	Model	1.5	0.81	3.5	23.6	20	27.6	0.16
	Full scale	20	3.5	9.81	22	20	23.9	0.16
SC8	Model	1.5	1.5	21	25.2	20	12	0.72
	Full scale	20	3.3	9.81	23	20	13	0.72

on 60% humidity and the temperature at building height for all cases. A zero-gradient boundary condition is set for pressure. Fig. 5 shows the approaching profiles for the cases under neutral and stable thermal stratification.

At the outlet, an *inletOutlet* condition is imposed for all variables except for pressure, for which a constant value of zero is set. At the top, zero-gradient conditions are used for temperature, the turbulent quantities and vapour concentration. A slip condition is set for velocity. At the lateral boundaries, a symmetric condition is applied to all variables. The ground and the buildings are modelled as solid walls, with the buildings considered as smooth surfaces (Ricci and Blocken, 2020). The water surface is also modelled as a wall and a smooth surface, assuming the absence of waves. It is worth stating this is a reasonable assumption as heatwaves are typically low wind speed phenomena. At the walls, the no-slip condition is applied for velocity, zero gradient is set for pressure, while wall functions are imposed for the turbulent quantities as described in Section 2.5.

4.4. Pollutant source

A hypothetical scenario is conceived according to which the open square represents an urban park without any traffic. Traffic, and thus sources of emission, is only assumed to exist in the four vertical street canyons. Therefore, a passive scalar is released from ground-

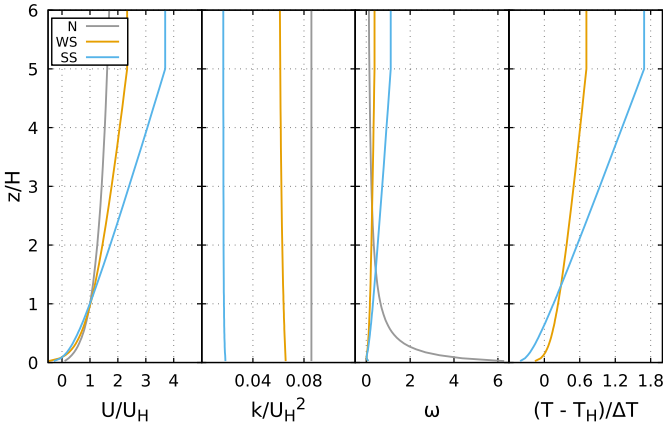

Fig. 5. Vertical profiles of U, k, ω and T of the approaching boundary layers for all cases. *N*: neutral conditions, *WS*: weak stability, *SS*: strong stability. The temperature profile for the neutral case is omitted as the respective simulations are initiated with a constant temperature value.

level line sources in both the upwind and downwind street canyons, as depicted in Fig. 1c. The ground is taken as the level of release to avoid any dependence of the results on the height of release and, thus, for the case to be generalisable (Indumati et al., 2009). The line sources are located in the middle of the street canyon with a width of two cells—or $0.17H$—in the x-direction and one cell—or $H/50$—in the z-direction. The lateral extent of the line sources is set equal to the entire lateral length of the street canyon. A constant pollutant flow rate is set for the ground cells belonging to the line sources. The pollutant parameters are set following *MC19*, where a mixture of air and propane is considered.

5. Results and discussion

First, the baseline cases without a waterbody are analysed. Horizontal profiles and contours are extracted at the pedestrian level ($z/H = 0.23$) corresponding to 1.75 m at full scale (Moonen et al., 2012; Ramponi et al., 2015). Three critical regions of interest are identified: (i) The open square, the area above and around the waterbody: $-1.5 \leq x/H \leq 1.5$ and $0 \leq y/H \leq 0.5$; (ii) Downwind canyons, the first and the second street canyon (in spanwise direction) downwind to the waterbody, namely DC1: $2.5 \leq x/H \leq 3.5$ and $0 \leq y/H \leq 0.5$; DC2: $4.5 \leq x/H \leq 5.5$ and $0 \leq y/H \leq 0.5$; (iii) The street canyon, with the axis in the streamwise direction, placed at the side of the open square: $-2.5 \leq x/H \leq 6.5$ and $0.5 \leq y/H \leq 1.5$.

5.1. Stability effects in the absence of waterbody

Fig. 6 displays the non-dimensional velocity magnitude and streamlines for the four baseline cases over a vertical plane at $y/H = 0$ in the open square. Based on Oke et al. (2017)'s classification, a typical isolated roughness flow regime is developed in the open square. Overall, the flow structure in all cases presents small differences, which is consistent with Guo et al. (2020). However, increased stability leads to a restricted main vortex closer to the ground, whereas a small additional vortex is formed on the upper left in the *MB* and *SB* cases. In the downwind canyons, a typical skimming flow structure is observed for all cases with a clockwise vortex present at the top-right part of the canyons. The effect of stability here is minimal, as also observed in *MC19*.

In Fig. 7, the profiles of the dimensionless and time-averaged streamwise (U) and vertical (W) velocities are plotted along three vertical lines within the open square and downwind canyons ($y/H = 0$). Globally, results show that stable stratification tends to increase streamwise velocity and decrease vertical motion due to the suppression of turbulence. Within the open square, the increase in stability leads to slightly increased U values in the upper part of the canyon along the centre and downwind lines, while in the downwind canyons, increased negative values are observed throughout the entire canyon height compared to the neutral case. For W, slightly decreased values are observed under stable stratification in the open square, as also found in Guo et al. (2020). However, the most significant effects are noticed in the downwind canyons where the *SB* case leads to almost zero vertical motion.

Fig. 8 depicts the velocity streamlines on a horizontal plane at pedestrian height ($z/H = 0.23$). The *NB* and *WB* cases present similar flow structures. A large anti-clockwise vortex is observed in the intersection of the open square with the street canyon, a small vortex is present in the upwind part of the open square and small recirculation areas are apparent further downwind in the street canyon. One notable difference is the strengthening of the main vortex in the *WB* case. Further increase in the background stability leads to large

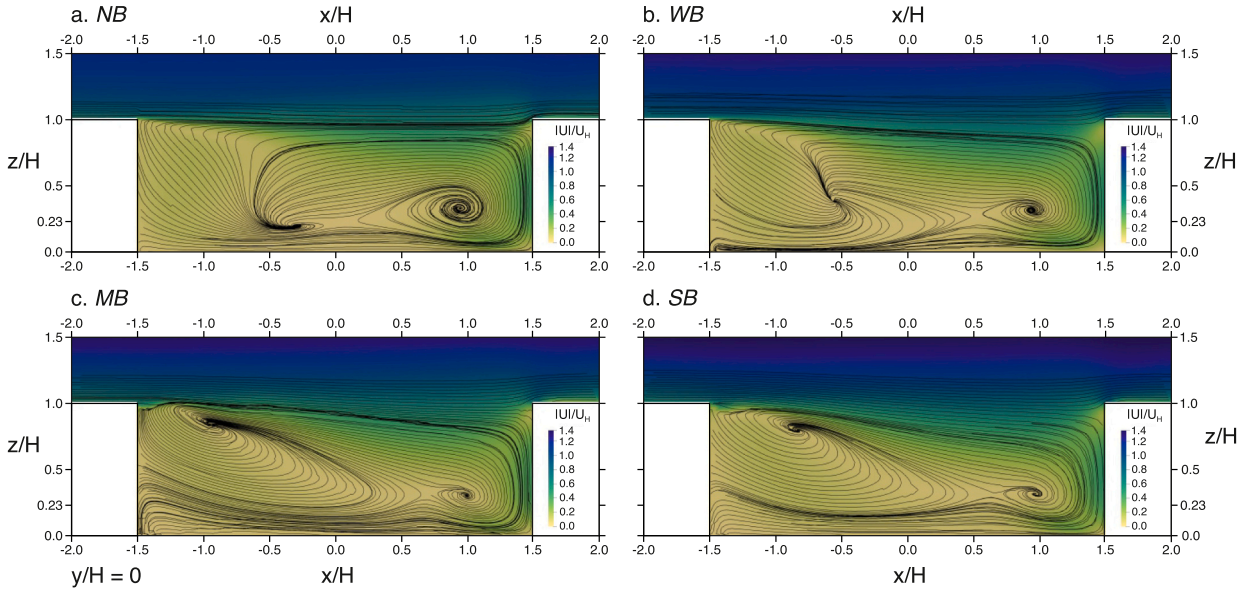

Fig. 6. Velocity streamlines for the baseline cases over a vertical plane at $y/H = 0$ in the open square ($-1.5 \leq x/H \leq 1.5$). Normalised velocity magnitude is depicted spatially in the background. (a) *NB*: neutral conditions baseline. (b) *WB*: weak stability baseline ($\zeta = 0.3$). (c) *MB*: medium stability baseline ($\zeta = 0.9$). (d) *SB*: strong stability baseline ($\zeta = 2.0$).

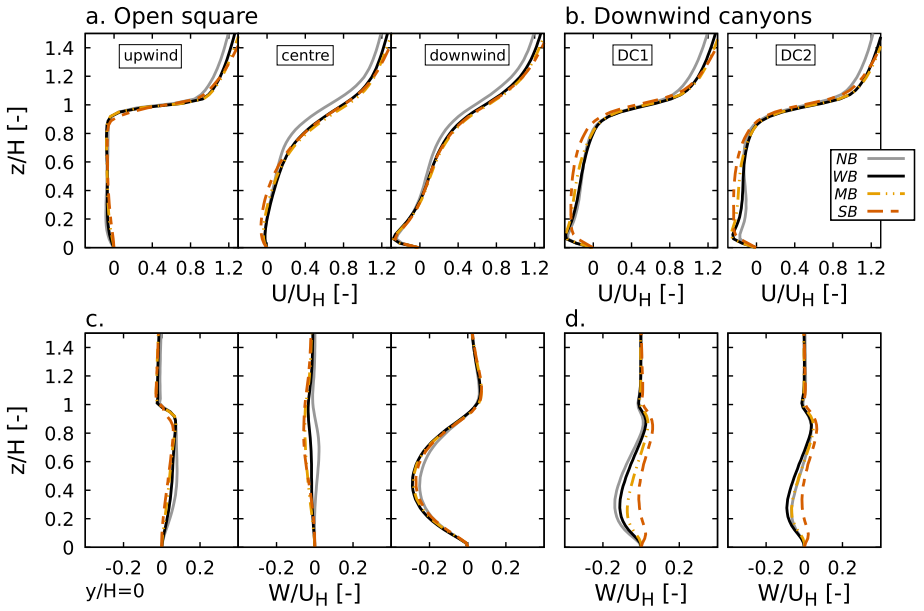

Fig. 7. Vertical profiles of (a,b) normalised streamwise velocity, U/U_H, and (c,d) normalised vertical velocity, W/U_H, along three vertical lines within the open square (upwind: $x/H = -1.13$; centre: $x/H = 0$; downwind: $x/H = 1.13$) and in the downwind canyons (located in the centreline of DC1: $x/H = 3$, and DC2: $x/H = 5$) at $y/H = 0$. Results for the four baseline cases.

discrepancies. In both *MB* and *SB* cases, the anti-clockwise vortex in the street canyon is disrupted, whilst the one near the upwind part of the open square is enhanced. All downwind canyons are now more isolated from the main flow compared to the situation observed in the *NB* and *WB* cases.

The results of the four baseline cases indicate that they share similar characteristics and that the main differences are observed between the *WB* and *SB* cases. Therefore, in the following, the discussion of the effects of stability is restricted to these two cases.

5.2. Blue space effects under stable stratification

Four cases with the presence of either a cooler ($\Delta T = -4^{\circ}$C and $\Delta T = -8^{\circ}$C) or warmer ($\Delta T = +4^{\circ}$C and $\Delta T = +8^{\circ}$C) waterbody are simulated for neutral, weak and strong background thermal stratification. A total of twelve simulations are presented here and discussed, comparing the results between them and against the baseline cases. A summary of the scaling quantities and the naming convention can be found in Table 3.

5.2.1. Mean velocity field

Fig. 9 depicts the velocity streamlines over a vertical plane passing from the centre of the open square. Under neutral conditions, the *NW*4 waterbody creates a thermal plume that enhances the principal vortex of the canyon—compared to the *NB* case in Fig. 6a—both in height and width. The warmer *NW*8 case increases velocities further and pushes the centre of the vortex higher up the canyon. Only a limited part of the flow breaks up the roof level. Under weak stability, the main vortex in the open square is further enhanced, and a new anti-clockwise vortex is formed close to the ground and near the upwind part of the waterbody. The *WW*4 and *WW*8 cases exhibit similar flow structures, albeit with an enhanced anti-clockwise vortex in the *WW*8 case. Overall, the induced upward buoyant flux is not strong enough to overcome the existing stable stratification that tends to suppress vertical motions. Under strong stability, the centre of the main vortex is pushed higher, while the vertical motion in the *SW*8 case is observed to slightly break the canyon-atmosphere interface ($z/H = 1$) near the downwind building. Although not shown here, it is worth noting that strong buoyant forces tend to decrease *U* values, with the most significant effects being observed in the *SW*4 and *SW*8 cases.

All cases in Fig. 9 have a Richardson number that ranges between $0.16 \leq Ri \leq 0.8$, with the highest values found for neutral conditions. In fact, for the two cases with the highest *Ri* number, that is the *NW*8 and *SW*8 cases, the slight breaking of the canyon-atmosphere interface is observed, highlighting the influence of the local convection regime. There is an indication that a *Ri* value close to unity would demonstrate more significant effects (Ampatzidis et al., 2022). Cool waterbodies have minimal impact on the in-canyon flow structure regardless of the strength of stability and water temperature; therefore the depiction of the streamlines for these cases is omitted. The impact of both warm and cool waterbodies, regardless of stability strength, on the flow structure of the downwind canyons is negligible compared to their baseline cases and therefore is not shown.

In Fig. 10, velocity streamlines for the warm-waterbody cases are shown over a horizontal plane at the pedestrian level. Both the $\Delta T = +4^{\circ}$C and $\Delta T = +8^{\circ}$C cases lead to similar results, so only the latter is shown. Compared to the flow structure of the baseline cases (Fig. 8), the *WW*8 case shows minimal impact, while the results of the *NW*8 and *SW*8 cases present some discrepancies. In the

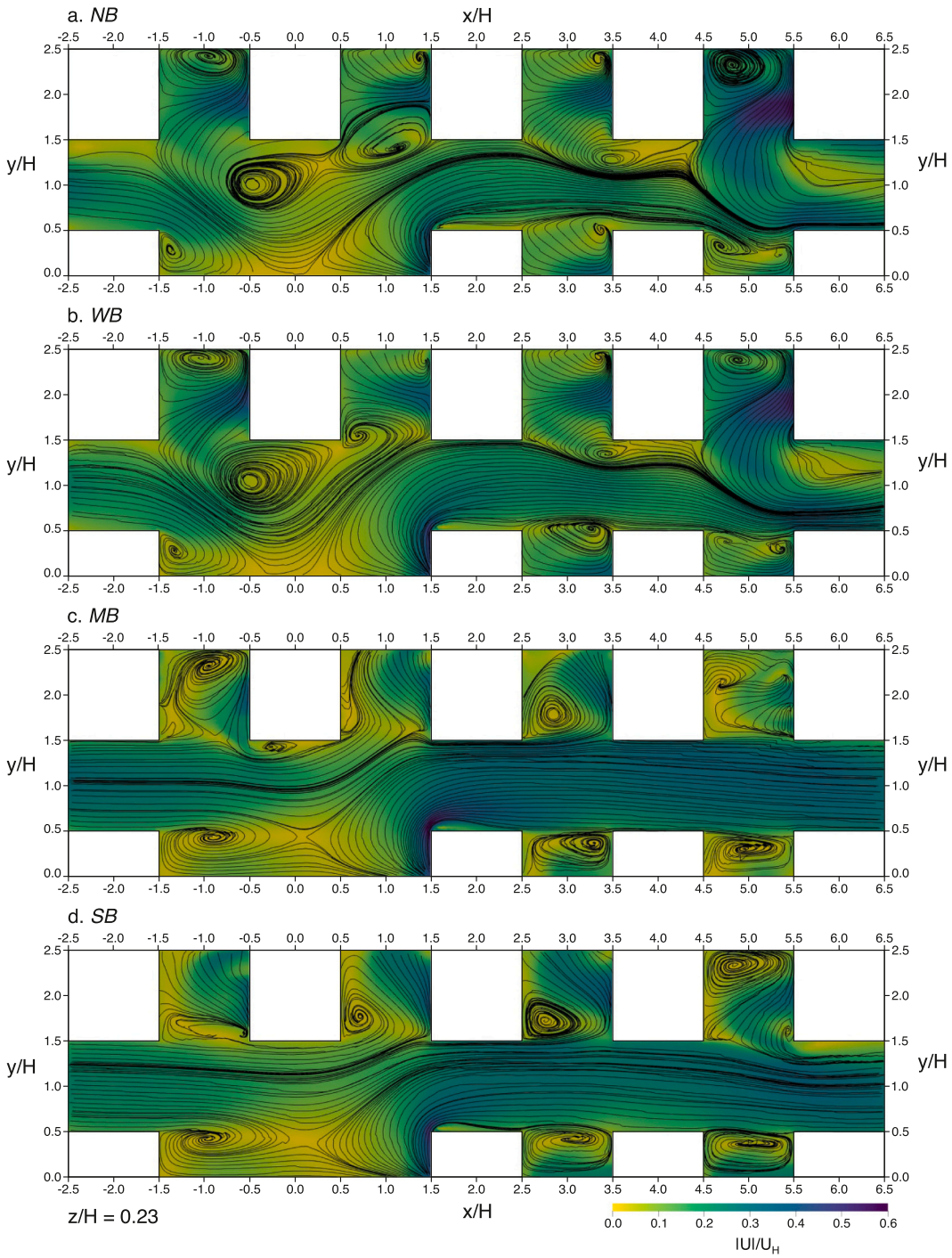

Fig. 8. Normalised streamwise velocity (U/U_H) along three vertical lines within the open square (upwind: $x/H = -1.13$; centre: $x/H = 0$; downwind: $x/H = 1.13$) and in the downwind canyons (located in the centreline of DC1: $x/H = 3$, and DC2: $x/H = 5$) at $y/H = 0$. Results for neutral conditions and the three stable thermal stratifications.

*NW*8 case, the main vortex in the street canyon is weakened, but the two secondary vortexes are destroyed. In the *SW*8 case, air flows almost linearly, leading to increased isolation of the downwind canyons from the primary flow. This is the result of the strong vertical motion causing air from the street canyon to be drawn towards the waterbody, altering the dynamics in the open square.

Fig. 11 shows the profiles of streamwise and spanwise velocity along the centreline of the street canyon $(y/H = 1)$ and at the pedestrian level. Cool waterbodies have minimal impact in all cases, albeit a slight decrease of *U* values in the open square under very

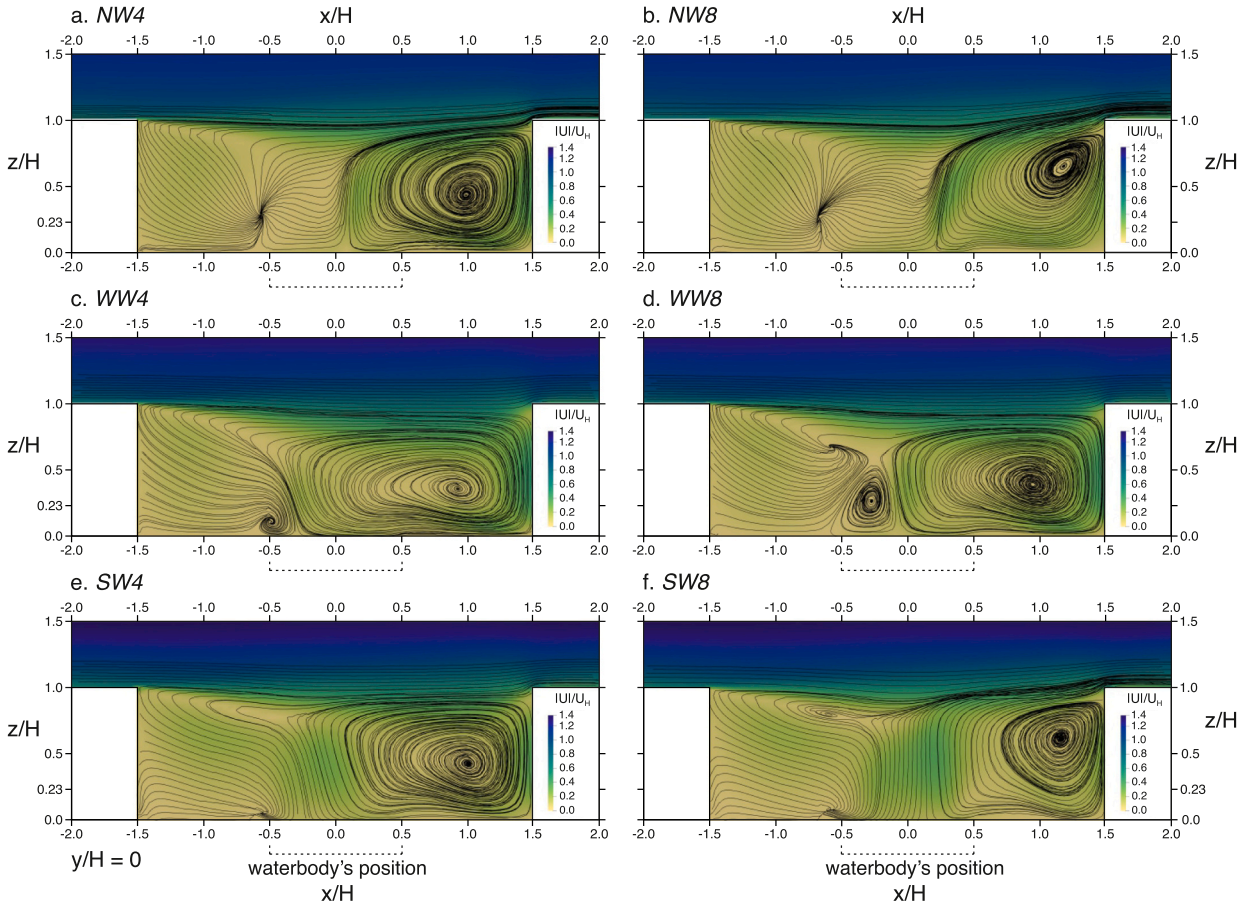

Fig. 9. Velocity streamlines over a vertical plane at $y/H = 0$ in the open square ($-1.5 \leq x/H \leq 1.5$). (a) *NW*4: neutral conditions, warm waterbody. (b) *NW*8: neutral conditions, warmer waterbody (c) *WW*4: weak stability, warm waterbody. (d) *WW*8: weak stability, warmer waterbody. (e) *SW*4: strong stability, warm waterbody. (f) *SW*8: strong stability, warmer waterbody. Warm waterbody: $\Delta T = +4^{\circ}$C. Warmer waterbody: $\Delta T = +8^{\circ}$C. The normalised velocity magnitude is depicted spatially in the background.

strong stability. For warm waterbodies, the neutral and very strong stability cases present the most significant effects. In the *NW*4 and *NW*8 cases, a velocity increase is observed in the downwind part of the open square and further downwind in the street canyon, while for the *SW*4 and *SW*8 cases a larger increase of U is noticed in the open square and a less significant effect further downwind. In addition, strong stability leads to an increase in U in the upwind-waterbody area. The influence of waterbodies ranges from negligible to slight changes for both strengths of stabilities for V. Warm waterbodies tend to slightly decrease V values in the downwind-waterbody area, with the neutral cases exhibiting a greater effect.

5.2.2. *Temperature field*

Temperature is normalised as $(T - T_H)/\mid T_H - T_w \mid$, where T_H and T_w are the temperatures of the air at building height and at water surface, respectively. T_H is estimated by averaging the temperatures in a horizontal plane at building height within the open square for the baseline cases. For cases under neutral conditions, T_H is equal to the air temperature applied at the inlet.

Fig. 12 depicts normalised temperature contours on a vertical plane at $y/H = 0$ for cases under neutral conditions. The results for the *NB* case are not shown given its uniform temperature distribution. The results of cool waterbodies demonstrate localised cooling effects above and around the water surface. The presence of warm waterbodies creates a thermal plume that is directed upwards and downwards, following the direction of the main flow, breaking the canyon-atmosphere interface in both cases. Compared to cases with a stronger mixed convection regime, such as the one presented in Ampatzidis et al. (2022) with $Ri = 1.1$, the effects are generally suppressed, highlighting the influence of local convection.

Fig. 13 depicts T^* contours for the baseline and warm-waterbody cases under weak and strong stability. The profiles of the cool waterbodies are similar to those in Fig. 12 and thus omitted. However, it should be noted that stability has suppressed their potential to cool the overlying air and the effects are restricted near the ground In the baseline cases, the temperature above the building is vertically stratified, while within the canyon, the temperature is inclined to be horizontally, rather than vertically, stratified, as warmer air sinks closer to the downwind wall and cooler air rises towards the roof level in the upwind part. This is in agreement with

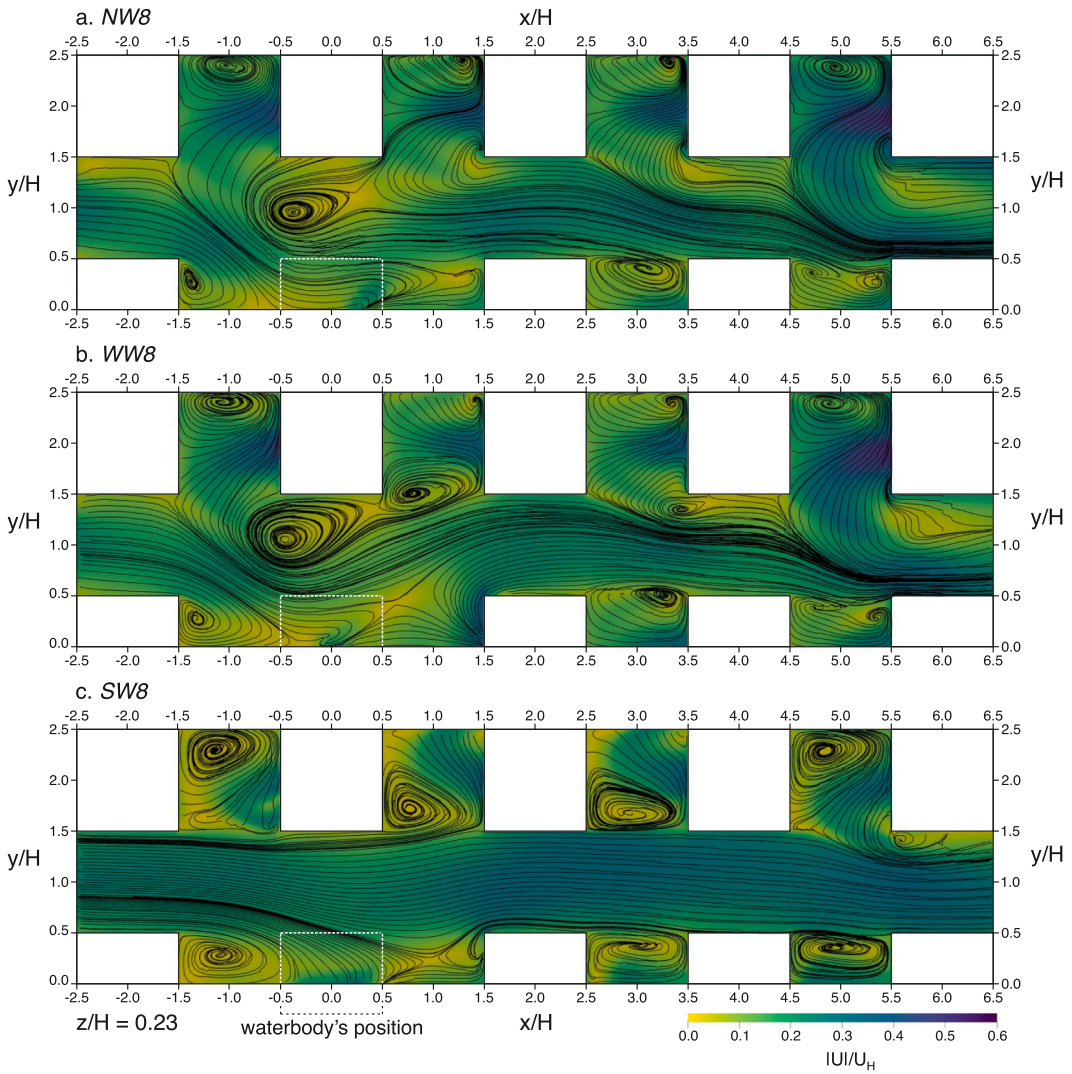

Fig. 10. Velocity streamlines for the cases of a warmer waterbody ($\Delta T = +8^{\circ}\mathrm{C}$) over a horizontal plane at the pedestrian level ($z/H = 0.23$).

the experiments of *MC19*. In the *SB* case, the $T^* = 0$ contour line is directed downwards near the downwind building, indicating that warmer air can reach lower heights within the open square. For the warm-waterbody cases, the strong vertical temperature gradient above water leads to the formation of an ascending buoyant flow, which is observed to reach greater heights in the warmer *WW*8 and *SW*8 cases. In almost all cases, air is trapped within the canyon and therefore the effects are distributed more widely across the open square compared to the results under neutral conditions. Only in the *SW*8 case, the strong upward motion seems to disrupt the roof-atmosphere interface, indicating that part of the in-canyon warm air is now being driven beyond roof level, albeit this effect is minimal.

For the analysis of the results in the horizontal plane and in order to be able to compare between different cases, we introduce the normalised temperature difference between the waterbody and the baseline cases: $TD^* = (T - T_b)/\mid T_H - T_w \mid$, where T_b is the temperature field of the baseline case. The employment of TD^* can help evaluate the total effectiveness, E_T, of blue space effects, i.e. the ratio between the total area of influence (A) and the waterbody area. The area of influence is defined as the area up to which convective effects are felt. The minimum threshold for estimating A is set to $TD^* = 0.01$. A distinction is made between the total effectiveness and the effectiveness of cooling, E_C, and warming, E_H.

For neutral conditions, Fig. 14 shows that cool waterbodies have a similar impact on the temperature field, whilst the *NW*8 case presents lower effectiveness and lower maximum TD^* value compared to the *NW*4. The latter can be attributed to the fact that more air is drawn upwards, leading to a decreased lateral influence.

Figs. 15–16 present horizontal TD^* contours for the cases with weak and strong stability. Cool waterbodies under weak stability present lower cooling effectiveness than under neutral conditions, with the cooling effects mostly restricted within the open square. As air is drawn towards the waterbody, a slight increase in temperature is observed in the downwind part of the street canyon. The warm waterbodies appear to have a more widespread effect across the entire building array. The *WW*4 presents the highest E_H, which is

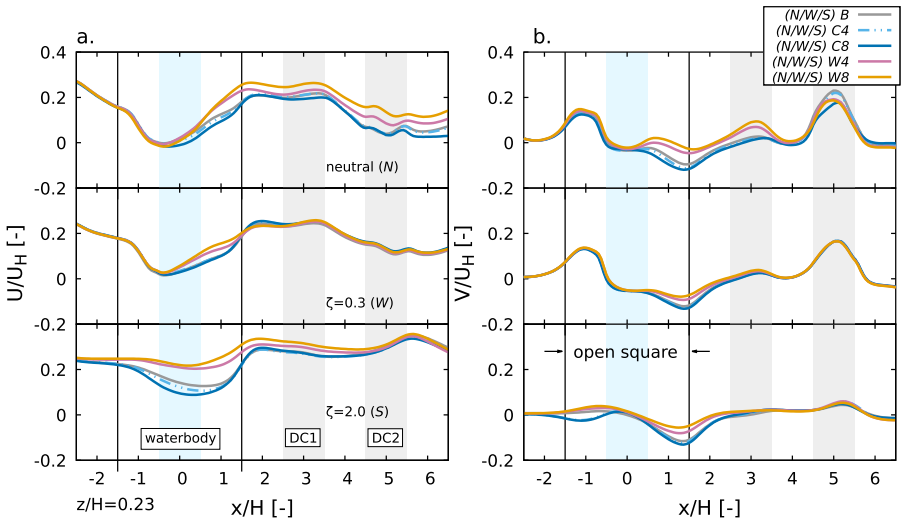

Fig. 11. Profiles of normalised (a) streamwise (U/U_H) and (b) spanwise (V/U_H) velocity over a horizontal line in the middle of the street canyon $(y/H = 1)$ at pedestrian level $(z/H = 0.23)$. The shaded areas denote the position of the waterbody (blue) and the downwind canyons DC1 and DC2 (grey). The location of the open square is shown with the vertical dotted lines. (For interpretation of the references to colour in this figure legend, the reader is referred to the web version of this article.)

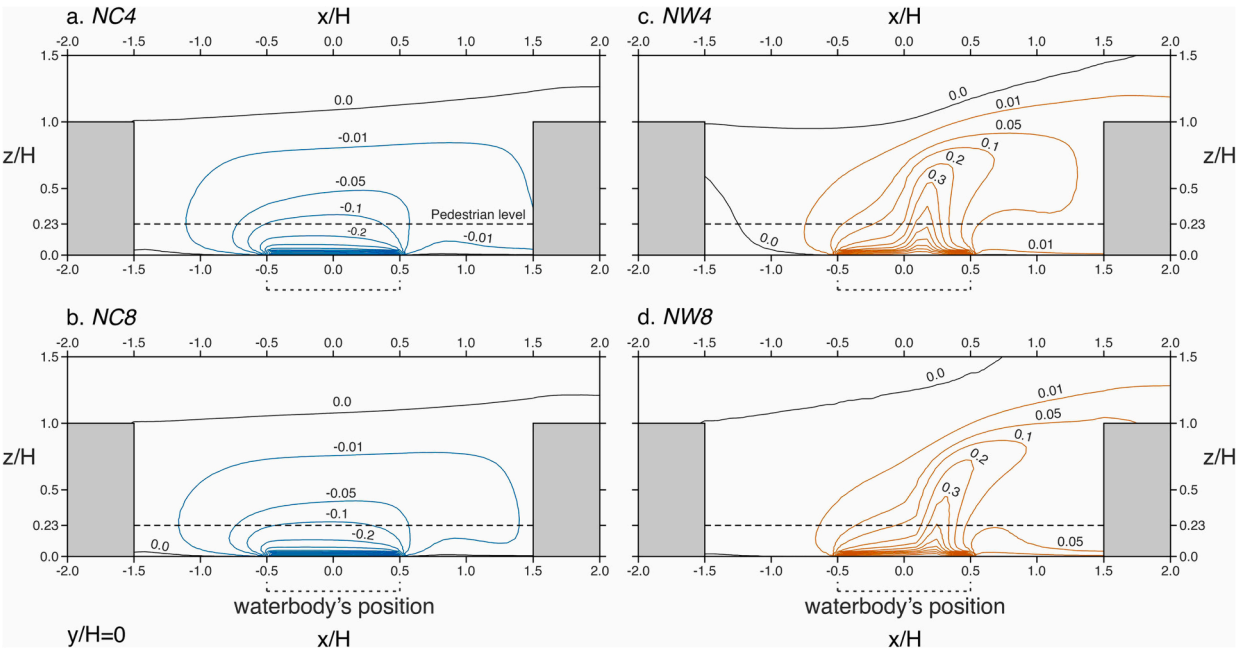

Fig. 12. Contours of normalised temperature (T^*) over a vertical plane in the middle of the open square $(y/H = 0)$ for the cases under neutral conditions. Blue and orange lines indicate a temperature greater and lower than the average temperature at building height, respectively. (For interpretation of the references to colour in this figure legend, the reader is referred to the web version of this article.)

approximately three times greater than the ones observed under neutral conditions.

Under strong stability (Fig. 16), waterbodies destabilise significantly the temperature field, leading to both warming and cooling effects being simultaneously present across the domain. The cooling effectiveness and maximum cooling effect are increased compared to neutral and weak stability cases, with the highest values observed in the *SC*8 case. At the same time, a strong warming effect with a lower effectiveness—compared to cooling—but with a maximum value of $TD^* = 0.76$ is noticed in the *SC*4 case. The warm waterbodies demonstrate a less widespread and less intense effect compared to weak stability cases, with the highest effectiveness $(E_H = 14.2)$ observed for the *SW*4 case. This can be explained by the formation of extended areas of decreased temperatures downwind of the

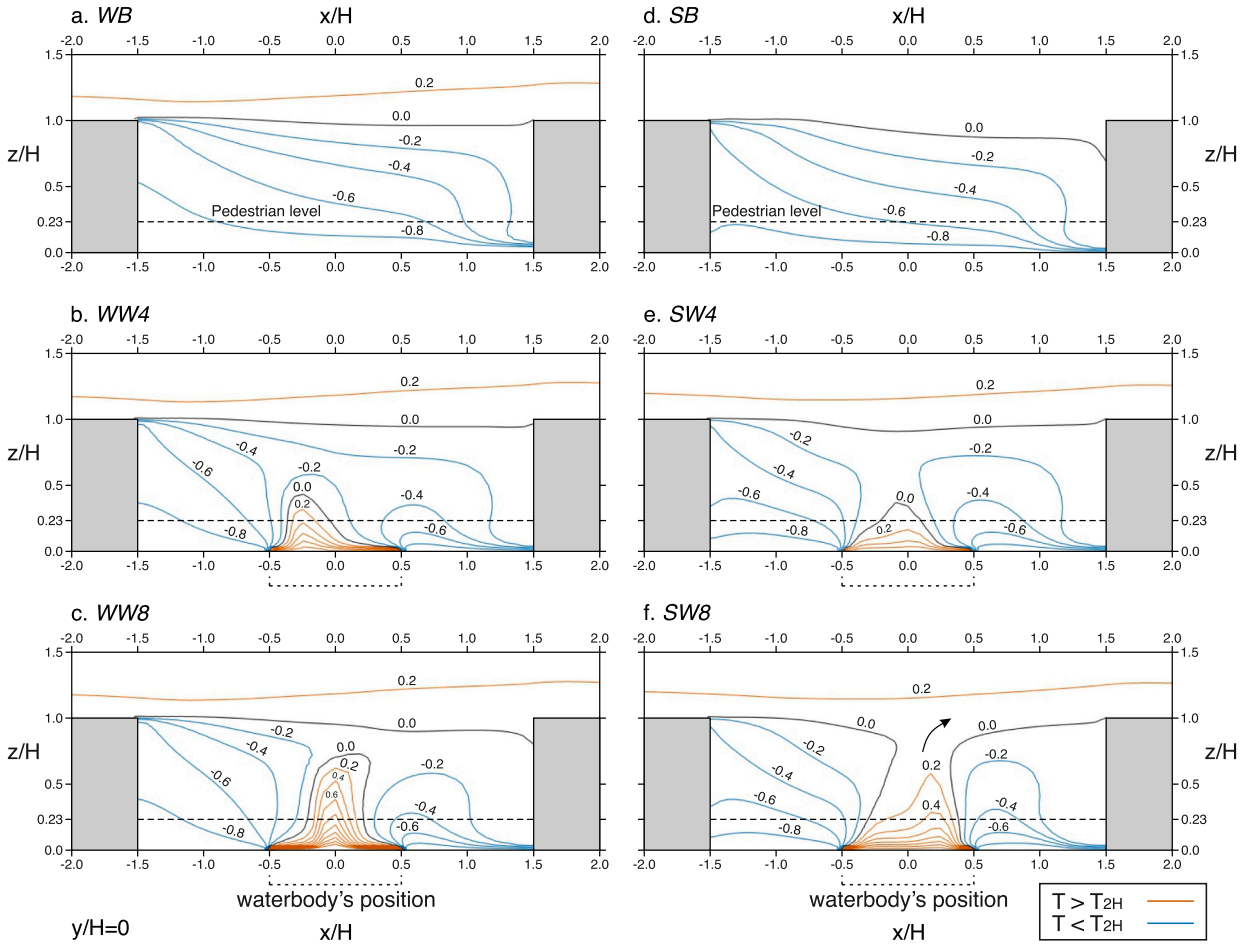

Fig. 13. Contours of normalised temperature (T^*) over a vertical plane in the middle of the open square ($y/H = 0$) for the cases under weak ($\zeta = 0.3$) and strong ($\zeta = 2.0$) stable background thermal stratification. Blue and orange lines indicate a temperature greater and lower than the average temperature at building height, respectively. (For interpretation of the references to colour in this figure legend, the reader is referred to the web version of this article.)

open square and in the individual canyons located above the street canyon that potentially prevent a more widespread warming effect. Note that the maximum cooling in these areas exceeds the values observed in *SC*4 and *SC*8, albeit with decreased effectiveness.

5.2.3. *Concentration of pollutants*

Fig. 17 shows the normalised concentration of pollutants (C^*) along three vertical lines in the open square and along the vertical centreline in the downwind canyons. The pollutant concentration is normalised as $C^* = CU_H H^2/Q$, where Q is the pollutant tracer flow rate from the source. The results show that for the baseline cases (without the waterbody), weak stability leads to increased C^* values in the open square, especially in the centre near the roof level and the entire downwind area. In the downwind canyons though, the changes are negligible. Under strong stability, a significant decrease in concentrations is observed in the open square, whereas a large increase can be seen in the downwind canyons. The presence of cool waterbodies has generally a limited impact in all cases, except for a slight increase in concentrations in the downwind part of the open square under neutral conditions and a decrease in C^* that is observed in the downwind canyons for the cooler waterbody under strong stability (*SC*8). Warm waterbodies have a more substantial influence. Under neutral conditions, a decrease in C^* is observed in the downwind part of the open square due to the breaking of the canopy layer as shown in Fig. 9. Under both weak and strong stability, warm waterbodies appear to increase concentrations in the open square, particularly near the ground.

In Fig. 18, the profiles of C^* are shown over a horizontal line in the middle of the street canyon ($y/H = 1$) and at pedestrian level. The results show that under neutral conditions and strong stability, cool waterbodies increase C^* in the open square but lead to lower values further downstream. The opposite is true for warm waterbodies, where decreased concentrations are observed across the entire horizontal street canyon. However, under weak stability, the induced buoyancy in the open square leads to increased concentration values in the downwind part of the horizontal street canyon.

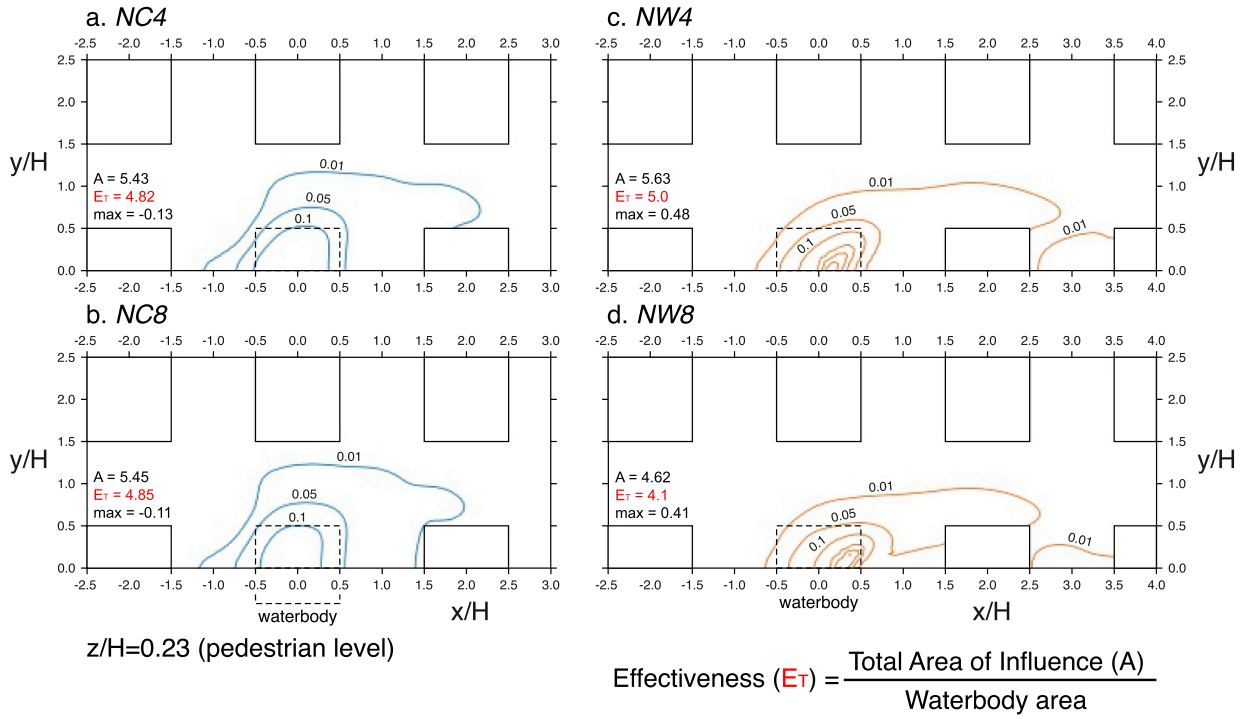

Fig. 14. Contours of normalised temperature difference (TD^*) over a horizontal plane at pedestrian height $(z/H = 0.23)$ for the cases under neutral conditions.

To assess the overall change in pollutant concentrations within the entire domain, the mean recirculation quotient is employed, as introduced by Göthe et al. (1988) and following similar work conducted by Cintolesi et al. (2021b) and Cheng and Liu (2011):

$$\Phi = \int_{Vol} C^* dV \Big/ \int_{Dom} C^* dV, \tag{17}$$

where C^* is integrated over the control volume (Vol) and over the entire domain (Dom). Five control volumes are identified to assess the recirculation of pollutants within the building array, as shown in Fig. 19a, measuring from the bottom to the roof level. The concentration of pollutants beyond the roof level is zero in all cases.

Fig. 19b depicts the recirculation quotients for the five identified control volumes. All baseline cases exhibit the highest concentrations in the *Street* volume, with decreasing magnitudes as the stability increases. This is due to the increased wind speeds that develop in the street canyon under strong stability. For the *SquareCanyon*, concentration increases under weak stability but drops for the strong stability case. This can be explained again by the high wind speeds under the *SB* that isolate the open square from the street canyon, thus, fewer pollutants enter the canyon. In the *SquareStreet* and DC1 canyon, Φ values are increasing with increasing stability, which supports the findings of *MC19*, while in *DC*2, a slight decrease of Φ can be observed.

In *SquareCanyon*, cool waterbodies lead to decreased Φ values for all cases with the most significant drop found for *SC*8 (−31%). Warm waterbodies lead to a considerable increase in Φ—up to 96% for *SW*8—due to the combination of two factors: the induced lateral flow towards the middle of the open square as a result of the upward motion but also the incapacity of the buoyant flow to break up the flow structure at roof level. A slight decrease in Φ is observed for the *NW*8 case (−4%) where the breaking of the canopy layer is most prominent. In *SquareStreet*, cool waterbodies lead to slightly increased concentration, except in the cases under strong stability. Warm waterbodies exhibit increased values because part of the main flow is directed towards the waterbody to replace the air that has moved upwards due to buoyancy. A small decrease in Φ is observed in the control volume *Street* for cool water bodies, except for a limited increase for *SC*8 (1.9%). However, the largest drop in Φ is caused by warm waterbodies under neutral conditions. In the downwind canyons, Φ is mostly dependent on the amount of air entering the canyon laterally, as the skimming flow is intact in all cases. Generally, cool waterbodies are observed to decrease concentrations—up to −24% for *NC*8 in DC2—whereas warm waterbodies lead to an increase—up to 101% for *NW*8 in DC1. A notable exception is the *SW*8 case where pollutant concentration is decreased in both canyons by up to 2%.

6. Conclusions

Investigating solutions that can simultaneously mitigate the UHI and alleviate the UPI is key to promoting sustainable cities that

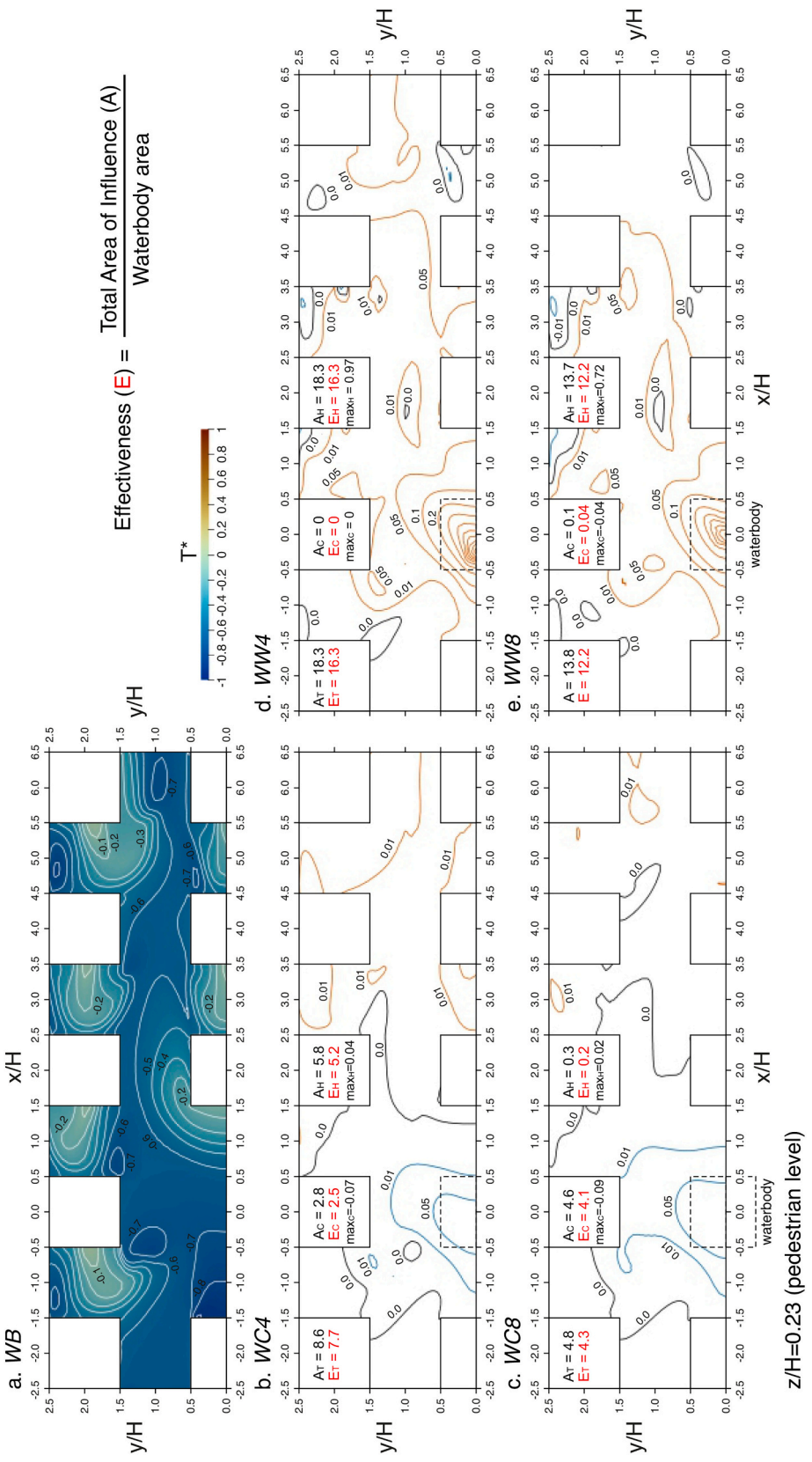

(caption on next page)

Fig. 15. (a) Normalised temperature (T^*) and (b,c,d,e) normalised temperature difference (TD^*) contours over a horizontal plane at pedestrian height ($z/H = 0.23$) for the cases under weak stability.

respond to climate change and promote human health. Stable atmospheric stratification, typical of heatwave events, exacerbates the heat island effect and increases the risk to human health and wellbeing. This paper attempts to appraise for the first time the mitigation effects induced by waterbodies within an idealised urban neighbourhood under such conditions using steady-state (RANS) simulations.

Results show that, in the presence of waterbodies, increased stability leads to the enhancement of the in-canyon principal vortex, resulting in a larger recirculation area in both height and width within the open square. Cool waterbodies induce a downward motion that pushes the flow laterally, while the thermal plume created by warm waterbodies leads to less widely spread effects. As a result, the cooler the waterbody, the greater its cooling effectiveness, whereas the warmer the waterbody, the less the area of influence, i.e. the distance up to which convective effects are felt. Note that increased stability has been shown to suppress the height up to which temperature effects are felt and leads to the formation of areas with both a cooling and warming effect.

A significant increase in the concentration of pollutants—up to ~100%, with the highest concentrations close to the ground—was observed in the open square under strong stability for warm waterbodies that do not generate a thermal plume strong enough to break the canopy layer, worsening the impact on human health. At the same time, the accumulation of pollutants in the open square led to lower concentrations in other parts of the domain, with the effect being more prominent under strong stability.

These findings highlight significant implications and provide new insights regarding the behaviour of waterbodies during heatwave events, which usually exhibit strong atmospheric stratification. It is suggested that in the morning and during the day, cool waterbodies can promote widespread cooling, while in the evenings and overnight, warm waterbodies can exacerbate heat stress and environmental conditions. But more than that, our findings demonstrate the complexity that characterises the interaction between waterbodies and the urban environment. It is clearly shown that not only do blue space effects depend on background stability conditions and the air-water temperature difference, but also that these effects are not restricted to the vicinity of waterbodies. These and previous findings indicate that the placement and size of urban blue space are key criteria when determining the overall resilience to climate change and the promotion of human health and wellbeing within a city. The methodology used in this paper approximated the waterbody as an evaporating surface and set temperature differences as a proxy for different parts of the diurnal cycle to examine the key impacts of atmospheric stratification on urban cooling and pollution dispersal. There remain however, questions about stratification of the waterbody and its level of thermal exchange with the surrounding urban context, which may form the basis of future work in this area, but can only be answered using much more computationally expensive multi-region simulations.

Funding

This work was supported by the Engineering and Physical Sciences Research Council (EPSRC)'Decarbonisation of the Built Environment' CDT with grant number EP/L016869/1 and the I-CHANGE project, funded by the European Union's Horizon 2020 research and innovation programme under grant agreement No. 101037193.

CRediT authorship contribution statement

Petros Ampatzidis: Conceptualization, Formal analysis, Investigation, Methodology, Software, Validation, Visualization, Writing – original draft, Writing – review & editing. **Carlo Cintolesi:** Methodology, Software, Writing – review & editing. **Silvana Di Sabatino:** Supervision, Writing – review & editing. **Tristan Kershaw:** Conceptualization, Supervision, Writing – review & editing.

Declaration of competing interest

The authors declare that they have no known competing financial interests or personal relationships that could have appeared to influence the work reported in this paper.

Data availability

Data will be made available on request.

Appendix A. Grid independence study

A grid independence study is conducted to assess the quality of the mesh. Three meshes are considered: (i) a medium mesh (the one finally selected for this study) with 2,033,440 cells; (ii) a coarse mesh with 246,640 cells and a refinement ratio of $r = 2.2$; (iii) a fine mesh composed of 7,002,720 cells and with a refinement ratio of $r = 1.8$. The representative cell lengths h, i.e. the average cell width estimated as the cube root of the cell volume, of the coarse, medium and fine mesh are 0.0029H, 0.0013H and 0.0007H. They all show more than 30% difference in h, as required by Celik et al. (2008).

Fig. A.20 presents the comparison of three target variables computed along a vertical line at the centre of the open square from the ground to roof level, i.e. mean values of dimensionless streamwise velocity (U/U_H), TKE ($k/{U_H}^2$) and concentration of pollutants (C^*), against the representative cell lengths of the three meshes. Using the Richardson extrapolation, the solution of an infinitely fine mesh is

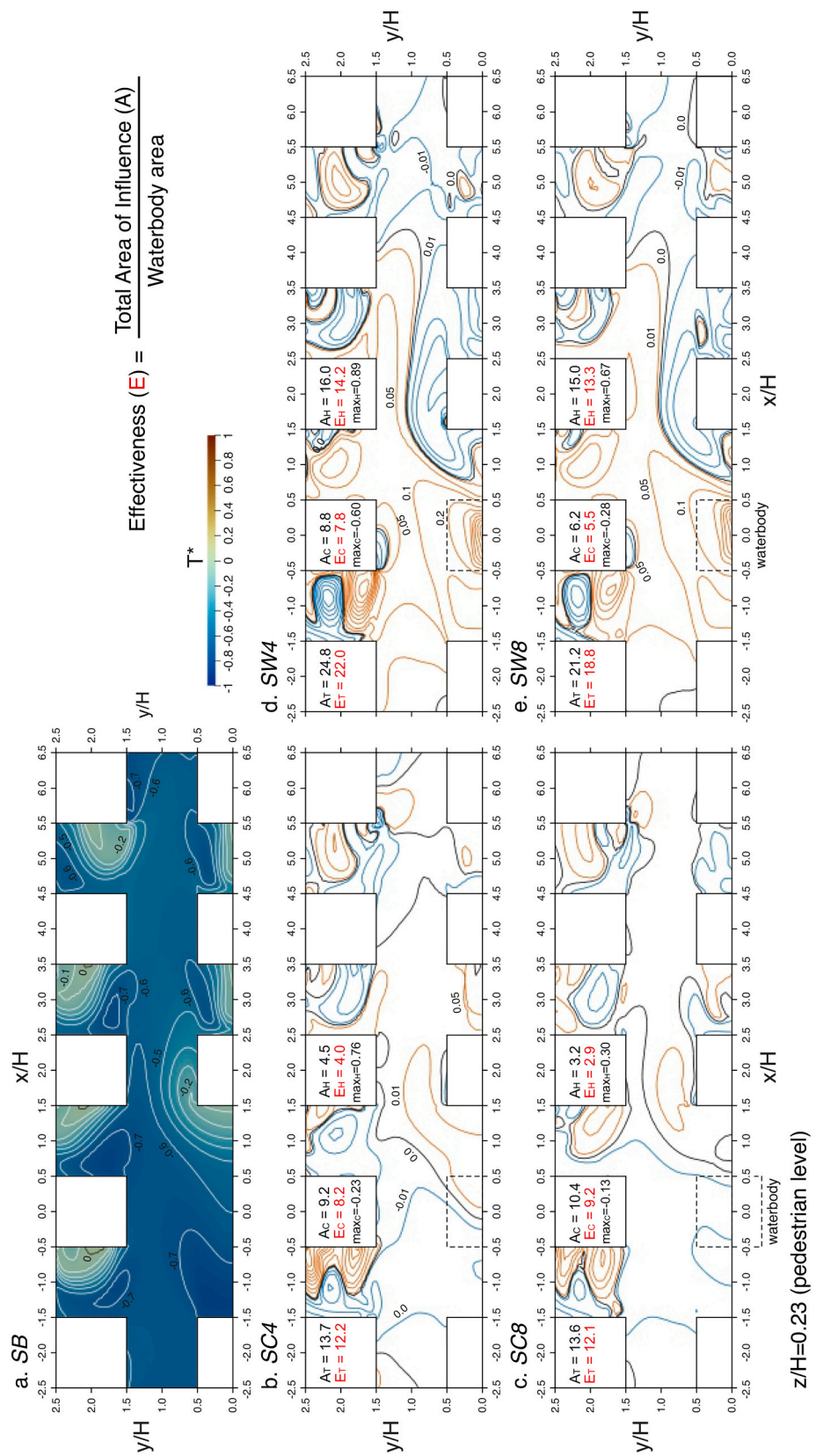

(caption on next page)

Fig. 16. (a) Normalised temperature (T^*) and (b,c,d,e) normalised temperature difference (TD^*) contours over a horizontal plane at pedestrian height ($z/H = 0.23$) for the cases under strong stability.

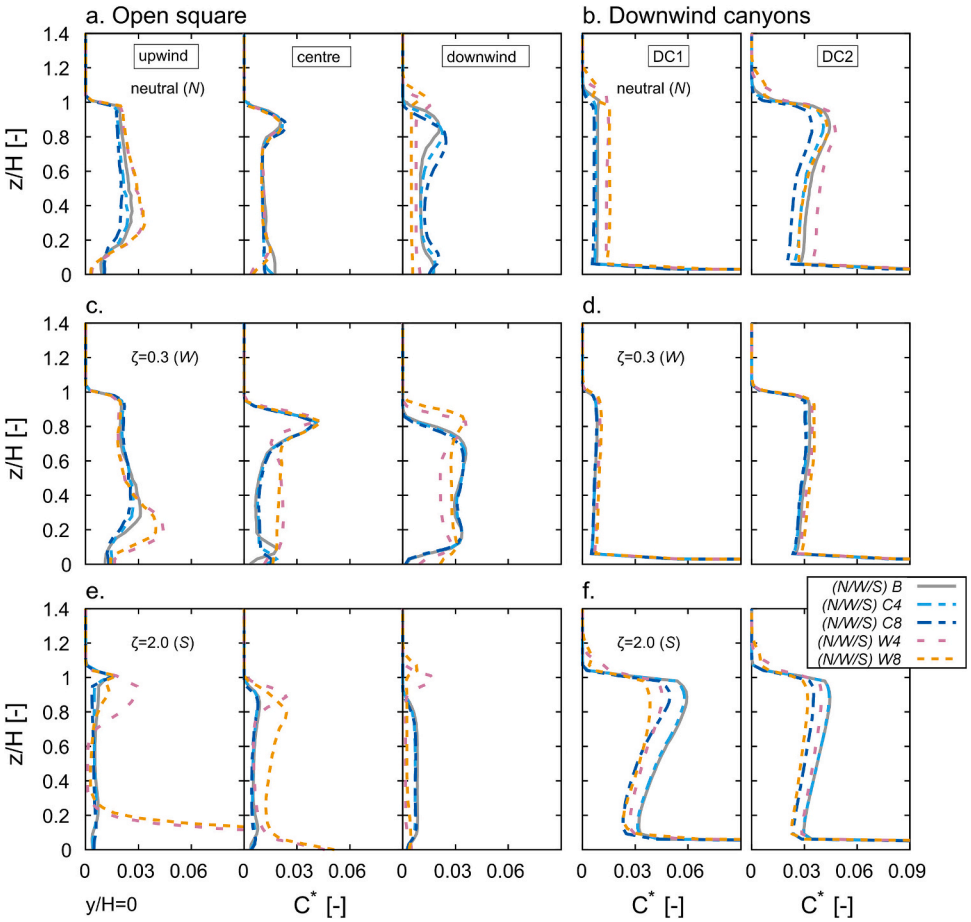

Fig. 17. Normalised pollutant concentration profiles (C^*) for the cases under neutral, weak and strong stability along three vertical lines within (a, b) the open square (upwind: $x/H = -1.13$; centre: $x/H = 0$; downwind: $x/H = 1.13$) and (c,d) the downwind canyons (located in the centreline of DC1: $x/H = 3$, and DC2: $x/H = 5$).

estimated on the basis of the values of the medium and fine mesh and is shown for $h = 0$. TKE and C^* exhibit monotonic convergence while U experiences oscillatory convergence. Results from the medium and fine meshes show values close to the solution for an infinitely fine mesh. The error estimate between the values of the medium and fine mesh is computed using the Grid Convergence Index (GCI) (Roache, 1994, 1997). GCI values for the U, TKE and C^* are 0.03%, 0.01% and 3%, respectively, indicating that the medium mesh provides nearly grid-independent results.

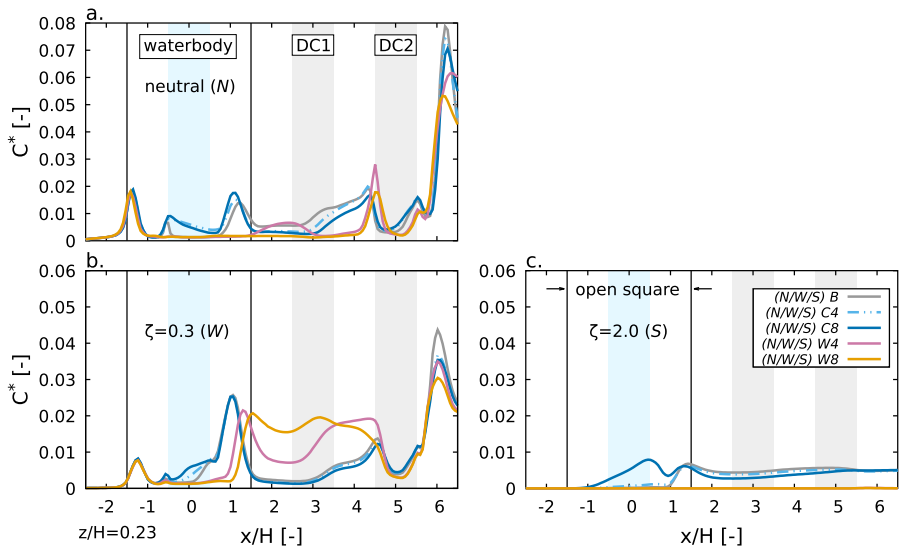

Fig. 18. Normalised pollutant concentration profiles (C^*) for the cases under (a) neutral conditions, (b) weak and strong stability along the centreline of the horizontal street canyon ($y/H = 1$) and at pedestrian height ($z/H = 0.23$).

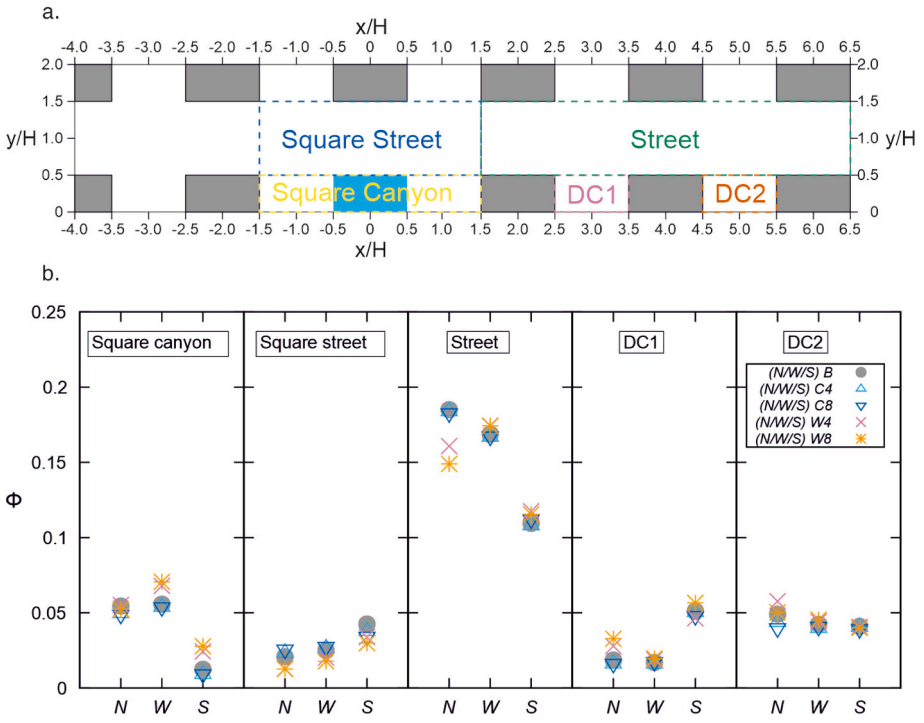

Fig. 19. (a) The five identified control volumes for the assessment of the recirculation of pollutants within the building array. In the vertical direction, each control volume ranges in $0 \leq z/H \leq 1$. Given the symmetry of the geometry, only half of the computational domain is considered. (b) Pollutant recirculation quotient, Φ, for the five selected control volumes.

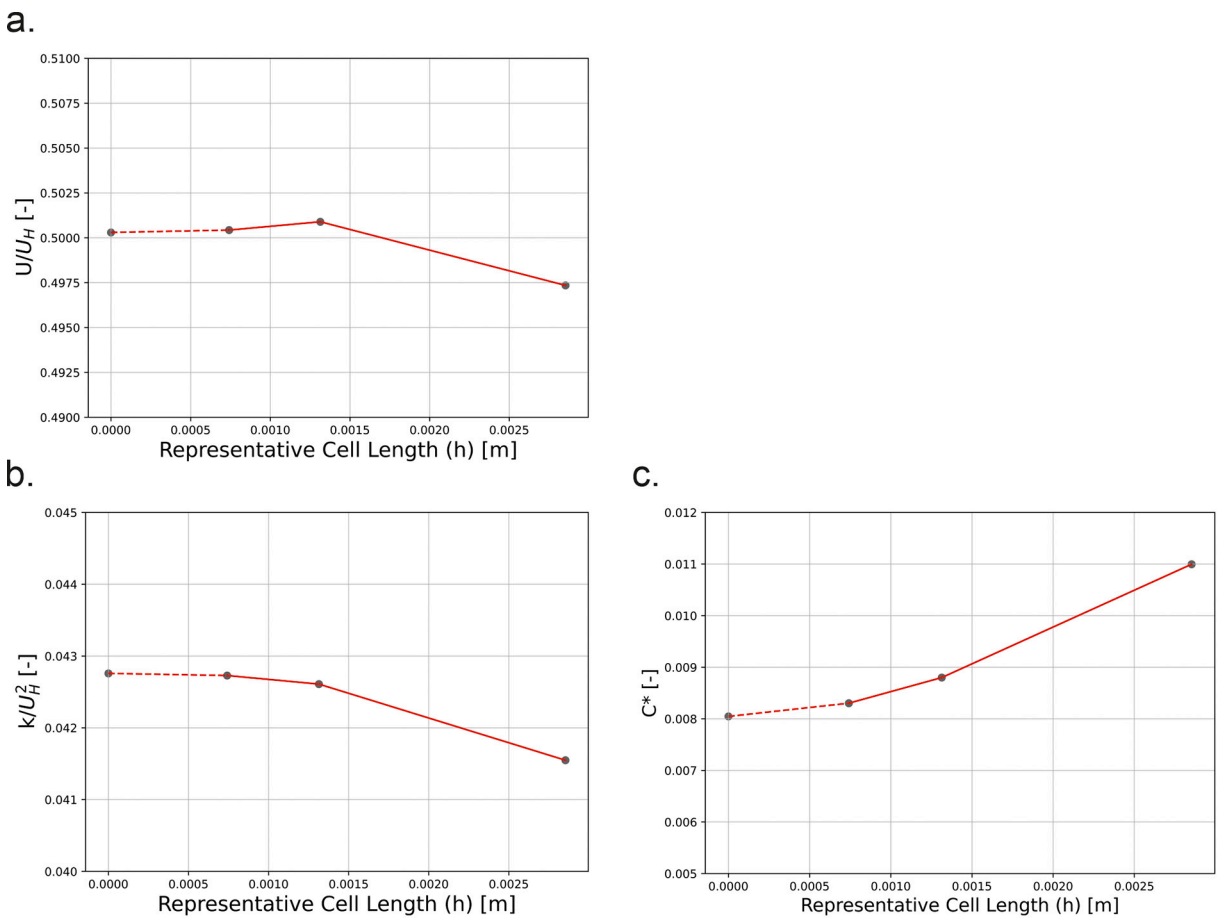

Fig. A.20. Results of the grid independence study for the non-isothermal case for mean values of (a) streamwise velocity (b) turbulent kinetic energy and (c) concentration of pollutants along a vertical line $(0 \leq z/H \leq 1)$ at $y/H = 0$ and $x/H = 0$.

References

Abhijith, K., Kumar, P., 2020. Quantifying particulate matter reduction and their deposition on the leaves of green infrastructure. Environ. Pollut. 265, 114884.

Abhijith, K., Kumar, P., Gallagher, J., McNabola, A., Baldauf, R., Pilla, F., Broderick, B., Di Sabatino, S., Pulvirenti, B., 2017. Air pollution abatement performances of green infrastructure in open road and built-up street canyon environments – a review. Atmos. Environ. 162, 71–86.

Allegrini, J., Dorer, V., Carmeliet, J., 2013. Wind tunnel measurements of buoyant flows in street canyons. Build. Environ. 59, 315–326.

Ampatzidis, P., Kershaw, T., 2020. A review of the impact of blue space on the urban microclimate. Sci. Total Environ. 730, 139068.

Ampatzidis, P., Cintolesi, C., Petronio, A., Di Sabatino, S., Kershaw, T., 2022. Evaporating waterbody effects in a simplified urban neighbourhood: a RANS analysis. J. Wind Eng. Ind. Aerodyn. 227, 105078.

Ampatzidis, P., Cintolesi, C., Kershaw, T., 2023. Impact of blue space geometry on urban heat island mitigation. Climate 11, 28.

Barbano, F., Brattich, E., Di Sabatino, S., 2021. Characteristic scales for turbulent exchange processes in a real urban canopy. Bound.-Layer Meteorol. 178, 119–142.

Boppana, V.B.L., Xie, Z.T., Castro, I.P., 2013. Large-eddy simulation of heat transfer from a single cube mounted on a very rough wall. Bound.-Layer Meteorol. 147, 347–368.

Buccolieri, R., Salim, S.M., Leo, L.S., Di Sabatino, S., Chan, A., Ielpo, P., de Gennaro, G., Gromke, C., 2011. Analysis of local scale tree–atmosphere interaction on pollutant concentration in idealized street canyons and application to a real urban junction. Atmos. Environ. 45, 1702–1713.

Celik, I.B., Ghia, U., Roache, P.J., Freitas, C.J., 2008. Procedure for estimation and reporting of uncertainty due to discretization in CFD applications. J. Fluids Eng. Trans. ASME 130.

Çengel, Y.A., Ghajar, A.J., 2015. Heat and Mass Transfer: Fundamentals & Applications. Fifth Edition in SI Units. McGraw-Hill Education.

Cheng, W.C., Liu, C.H., 2011. Large-eddy simulation of flow and pollutant transports in and above two-dimensional idealized street canyons. Bound.-Layer Meteorol. 139, 411–437.

Cintolesi, C., Petronio, A., Armenio, V., 2016. Large-eddy simulation of thin film evaporation and condensation from a hot plate in enclosure: first order statistics. Int. J. Heat Mass Transf. 101, 1123–1137.

Cintolesi, C., Petronio, A., Armenio, V., 2017. Large-eddy simulation of thin film evaporation and condensation from a hot plate in enclosure: second order statistics. Int. J. Heat Mass Transf. 115, 410–423.

Cintolesi, C., Barbano, F., Di Sabatino, S., 2021a. Large-eddy simulation analyses of heated urban canyon facades. Energies 14, 3078.

Cintolesi, C., Pulvirenti, B., Di Sabatino, S., 2021b. Large-eddy simulations of pollutant removal enhancement from urban canyons. Bound.-Layer Meteorol. 180, 79–104.

Crutzen, P.J., 2004. New directions: the growing urban heat and pollution "island" effect – impact on chemistry and climate. Atmos. Environ. 38, 3539–3540.

Debele, S.E., Leo, L.S., Kumar, P., Sahani, J., Ommer, J., Bucchignani, E., Vranić, S., Kalas, M., Amirzada, Z., Pavlova, I., Shah, M.A.R., Gonzalez-Ollauri, A., Di Sabatino, S., 2023. Nature-based solutions can help reduce the impact of natural hazards: a global analysis of nbs case studies. Sci. Total Environ. 902, 165824.
Di Sabatino, S., Buccolieri, R., Pulvirenti, B., Britter, R., 2007. Simulations of pollutant dispersion within idealised urban-type geometries with cfd and integral models. Atmos. Environ. 41, 8316–8329.
Di Sabatino, S., Barbano, F., Brattich, E., Pulvirenti, B., 2020. The multiple-scale nature of urban heat island and its footprint on air quality in real urban environment. Atmosphere 11, 1186.
EEA, 2022. Air Quality in Europe 2022. Technical Report. European Environment Agency (EEA).
Environmental Audit, 2018. Heatwaves: adapting to climate change. web: https://publications.parliament.uk/pa/cm201719/cmselect/cmenvaud/826/82603.htm. Accessed on 01.11.2022.
ESI-OpenCFD, 2006. OpenFOAM®, OpenCFD Ltd Release version 2006. web: https://www.openfoam.com/news/main-news/openfoam-v20-06. Accessed on 03.01.2022.
Fan, Z., Zhan, Q., Liu, H., Wu, Y., Xia, Y., 2022. Investigating the interactive and heterogeneous effects of green and blue space on urban PM2.5 concentration, a case study of Wuhan. J. Clean. Prod. 378, 134389.
Franke, J., Hellsten, A., Schlünzen, H., Carissimo, B., 2007. Best practice guideline for the CFD simulation of flows in the urban environment. COST Action 732.
Frantzeskaki, N., McPhearson, T., Collier, M.J., Kendal, D., Bulkeley, H., Dumitru, A., Walsh, C., Noble, K., van Wyk, E., Ordóñez, C., Oke, C., Pintér, L., 2019. Nature-based solutions for urban climate change adaptation: linking science, policy, and practice communities for evidence-based decision-making. BioScience 69, 455–466.
Girardin, C.A., Jenkins, S., Seddon, N., Allen, M., Lewis, S.L., Wheeler, C.E., Griscom, B.W., Malhi, Y., 2021. Nature-based solutions can help cool the planet—if we act now. Nature 593, 191–194.
Göthe, C.J., Bjurström, R., Ancker, K., 1988. A simple method of estimating air recirculation in ventilation systems. Am. Ind. Hyg. Assoc. J. 49, 66–69.
Grylls, T., Suter, I., van Reeuwijk, M., 2020. Steady-state large-eddy simulations of convective and stable urban boundary layers. Bound.-Layer Meteorol. 175, 309–341.
Gunawardena, K., Wells, M., Kershaw, T., 2017. Utilising green and bluespace to mitigate urban heat island intensity. Sci. Total Environ. 584-585, 1040–1055.
Guo, D., Zhao, P., Wang, R., Yao, R., Hu, J., 2020. Numerical simulations of the flow field and pollutant dispersion in an idealized urban area under different atmospheric stability conditions. Process. Saf. Environ. Prot. 136, 310–323.
Guo, D., Yang, F., Shi, X., Li, Y., Yao, R., 2021. Numerical simulation and wind tunnel experiments on the effect of a cubic building on the flow and pollutant diffusion under stable stratification. Build. Environ. 205, 108222.
Indumati, S., Oza, R., Mayya, Y., Puranik, V., Kushwaha, H., 2009. Dispersion of pollutants over land–water–land interface: study using CALPUFF model. Atmos. Environ. 43, 473–478.
Kadaverugu, R., Dhyani, S., Dasgupta, R., Kumar, P., Matli, C., 2022. Urban sustainability and resilience building: Blue-green infrastructure for air pollution abatement and realizing multiple co-benefits. In: Blue-Green Infrastructure across Asian Countries: Improving Urban Resilience and Sustainability. Springer Singapore, Singapore, pp. 397–417.
Kanda, I., Yamao, Y., 2016. Passive scalar diffusion in and above urban-like roughness under weakly stable and unstable thermal stratification conditions. J. Wind Eng. Ind. Aerodyn. 148, 18–33.
Li, X.X., Britter, R.E., Koh, T.Y., Norford, L.K., Liu, C.H., Entekhabi, D., Entekhabi, D., 2010. Large-eddy simulation of flow and pollutant transport in urban street canyons with ground heating. Bound.-Layer Meteorol. 137, 187–204.
Li, H., Meier, F., Lee, X., Chakraborty, T., Liu, J., Schaap, M., Sodoudi, S., 2018. Interaction between urban heat island and urban pollution island during summer in Berlin. Sci. Total Environ. 636, 818–828.
Lyons, W.A., Olsson, L.E., 1973. Detailed mesometeorological studies of air pollution dispersion in the Chicago lake breeze. Mon. Weather Rev. 101, 387–403.
Marucci, D., Carpentieri, M., 2019. Effect of local and upwind stratification on flow and dispersion inside and above a bi-dimensional street canyon. Build. Environ. 156, 74–88.
Marucci, D., Carpentieri, M., 2020a. Dispersion in an array of buildings in stable and convective atmospheric conditions. Atmos. Environ. 222, 117100.
Marucci, D., Carpentieri, M., 2020b. Stable and convective boundary-layer flows in an urban array. J. Wind Eng. Ind. Aerodyn. 200, 104140.
Marucci, D., Carpentieri, M., Hayden, P., 2018. On the simulation of thick non-neutral boundary layers for urban studies in a wind tunnel. Int. J. Heat Fluid Flow 72, 37–51.
Menter, F., Kuntz, M., Langtry, R., 2003. Ten years of industrial experience with the sst turbulence model. In: Proceedings of the fourth International Symposium on Turbulence, Heat and Mass Transfer, pp. 625–632.
Moonen, P., Defraeye, T., Dorer, V., Blocken, B., Carmeliet, J., 2012. Urban physics: effect of the micro-climate on comfort, health and energy demand. Front. Archit. Res. 1, 197–228.
Oke, T.R., Mills, G., Christen, A., Voogt, J.A., 2017. Urban Climates. Cambridge University Press.
Pauken, M.T., 1998. An experimental investigation of combined turbulent free and forced evaporation. Exp. Thermal Fluid Sci. 18, 334–340.
Petronio, A., 2010. Numerical Investigation of Condensation and Evaporation Effects inside a Tub. Ph.D. thesis.. School of Environmental and Industrial Fluid Mechanics, University of Trieste.
Pope, S.B., 2013. Turbulent Flows. Taylor & Francis, London.
Ramponi, R., Blocken, B., de Coo, L.B., Janssen, W.D., 2015. CFD simulation of outdoor ventilation of generic urban configurations with different urban densities and equal and unequal street widths. Build. Environ. 92, 152–166.
Ricci, A., Blocken, B., 2020. On the reliability of the 3D steady RANS approach in predicting microscale wind conditions in seaport areas: the case of the IJmuiden Sea lock. J. Wind Eng. Ind. Aerodyn. 207, 104437.
Richards, P., Hoxey, R., 1993. Appropriate boundary conditions for computational wind engineering models using the $k-\varepsilon$ turbulence model. J. Wind Eng. Ind. Aerodyn. 46-47, 145–153. Proceedings of the 1st international on computational wind engineering.
Richards, P., Norris, S., 2011. Appropriate boundary conditions for computational wind engineering models revisited. J. Wind Eng. Ind. Aerodyn. 99, 257–266. The Fifth International Symposium on Computational Wind Engineering.
Roache, P.J., 1994. Perspective: a method for uniform reporting of grid refinement studies. J. Fluids Eng. Trans. ASME 116.
Roache, P.J., 1997. Quantification of uncertainty in computational fluid dynamics. Annu. Rev. Fluid Mech. 29, 123–160.
Roth, M., 2000. Review of atmospheric turbulence over cities. Q. J. R. Meteorol. Soc. 126, 941–990.
Salim, S.M., Buccolieri, R., Chan, A., Di Sabatino, S., 2011. Numerical simulation of atmospheric pollutant dispersion in an urban street canyon: comparison between rans and les. J. Wind Eng. Ind. Aerodyn. 99, 103–113.
Santamouris, M., 2015. Analyzing the heat island magnitude and characteristics in one hundred Asian and Australian cities and regions. Sci. Total Environ. 512-513, 582–598.
Schatzmann, M., Olesen, H., Franke, J., 2010. COST 732 Model Evaluation Case Studies: Approach and Results. Technical Report. COST Office.
Schrijvers, P., Jonker, H., Kenjereš, S., de Roode, S., 2015. Breakdown of the night time urban heat island energy budget. Build. Environ. 83, 50–64 (Special Issue: Climate adaptation in cities).
Selmi, W., Weber, C., Rivière, E., Blond, N., Mehdi, L., Nowak, D., 2016. Air pollution removal by trees in public green spaces in Strasbourg city, France. Urban For. Urban Green. 17, 192–201.
Sessa, V., Xie, Z.T., Herring, S., 2020. Thermal stratification effects on turbulence and dispersion in internal and external boundary layers. Bound.-Layer Meteorol. 176, 61–83.
Sosnowski, P., Petronio, A., Armenio, V., 2013. Numerical model for thin liquid film with evaporation and condensation on solid surfaces in systems with conjugated heat transfer. Int. J. Heat Mass Transf. 66, 382–395.

Tominaga, Y., Mochida, A., Yoshie, R., Kataoka, H., Nozu, T., Yoshikawa, M., Shirasawa, T., 2008. AIJ guidelines for practical applications of CFD to pedestrian wind environment around buildings. J. Wind Eng. Ind. Aerodyn. 96, 1749–1761, 4th International Symposium on Computational Wind Engineering (CWE2006).

Tsalicoglou, C., Allegrini, J., Carmeliet, J., 2020. Non-isothermal flow between heated building models. J. Wind Eng. Ind. Aerodyn. 204, 104248.

UKHSA, 2022. UK Health Security Agency. Heatwave plan for England: Protecting health and reducing harm from severe heat and heatwaves. https://www.gov.uk/government/publications/heatwave-plan-for-england. accessed: 14.12.2023.

Watts, N., Amann, M., Arnell, N., Ayeb-Karlsson, S., Beagley, J., Belesova, K., Boykoff, M., Byass, P., Cai, W., Campbell-Lendrum, D., Capstick, S., Chambers, J., Coleman, S., Dalin, C., Daly, M., Dasandi, N., Dasgupta, S., Davies, M., Di Napoli, C., Dominguez-Salas, P., Drummond, P., Dubrow, R., Ebi, K.L., Eckelman, M., Ekins, P., Escobar, L.E., Georgeson, L., Golder, S., Grace, D., Graham, H., Haggar, P., Hamilton, I., Hartinger, S., Hess, J., Hsu, S.C., Hughes, N., Jankin Mikhaylov, S., Jimenez, M.P., Kelman, I., Kennard, H., Kiesewetter, G., Kinney, P.L., Kjellstrom, T., Kniveton, D., Lampard, P., Lemke, B., Liu, Y., Liu, Z., Lott, M., Lowe, R., Martinez-Urtaza, J., Maslin, M., McAllister, L., McGushin, A., McMichael, C., Milner, J., Moradi-Lakeh, M., Morrissey, K., Munzert, S., Murray, K.A., Neville, T., Nilsson, M., Sewe, M.O., Oreszczyn, T., Otto, M., Owfi, F., Pearman, O., Pencheon, D., Quinn, R., Rabbaniha, M., Robinson, E., Rocklöv, J., Romanello, M., Semenza, J.C., Sherman, J., Shi, L., Springmann, M., Tabatabaei, M., Taylor, J., Triñanes, J., Shumake-Guillemot, J., Vu, B., Wilkinson, P., Winning, M., Gong, P., Montgomery, H., Costello, A., 2021. The 2020 report of the lancet countdown on health and climate change: responding to converging crises. Lancet 397, 129–170.

Welty, J., Wicks, C., Rorrer, G., Wilson, R., 2007. Fundamentals of Momentum, Heat and Mass Transfer. Wiley.

Wu, S., Luo, M., Zhao, R., Li, J., Sun, P., Liu, Z., Wang, X., Wang, P., Zhang, H., 2023. Local mechanisms for global daytime, nighttime, and compound heatwaves. npj Clim. Atmos. Sci. 6, 36.

Xie, Z.T., Hayden, P., Wood, C.R., 2013. Large-eddy simulation of approaching-flow stratification on dispersion over arrays of buildings. Atmos. Environ. 71, 64–74.

Yao, L., Sailor, D.J., Zhang, X., Wang, J., Zhao, L., Yang, X., 2023. Diurnal pattern and driving mechanisms of the thermal effects of an urban pond. Sustain. Cities Soc. 91, 104407.

Yassin, M.F., 2013. A wind tunnel study on the effect of thermal stability on flow and dispersion of rooftop stack emissions in the near wake of a building. Atmos. Environ. 65, 89–100.

Zhao, Y., Chew, L.W., Kubilay, A., Carmeliet, J., 2020. Isothermal and non-isothermal flow in street canyons: a review from theoretical, experimental and numerical perspectives. Build. Environ. 184, 107163.

Zhao, L., Li, T., Przybysz, A., Guan, Y., Ji, P., Ren, B., Zhu, C., 2021. Effect of urban lake wetlands and neighboring urban greenery on air PM10 and PM2.5 mitigation. Build. Environ. 206, 108291.

Zhou, X., Ying, A., Cong, B., Kikumoto, H., Ooka, R., Kang, L., Hu, H., 2021. Large eddy simulation of the effect of unstable thermal stratification on airflow and pollutant dispersion around a rectangular building. J. Wind Eng. Ind. Aerodyn. 211, 104526.